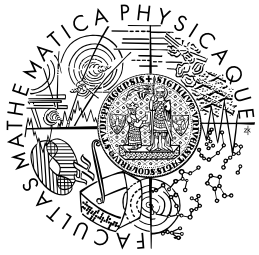

FACULTY
OF MATHEMATICS
AND PHYSICS
Charles University

MASTER THESIS

Bc. Marek Martaus

Tests of Semiconductor Detectors for ATLAS Upgrade

Institute of particle and nuclear physics

Supervisor of the master thesis: doc. RNDr. Peter Kodyš, CSc.
Study programme: Physics
Study branch: Nuclear and Particle Physics

Prague 2021

I declare that I carried out this master thesis independently, and only with the cited sources, literature and other professional sources. It has not been used to obtain another or the same degree.

I understand that my work relates to the rights and obligations under the Act No. 121/2000 Sb., the Copyright Act, as amended, in particular the fact that the Charles University has the right to conclude a license agreement on the use of this work as a school work pursuant to Section 60 subsection 1 of the Copyright Act.

In Prague, January 3rd, 2021 .....

Author's signature

First of all, I would like to mention the supervisor doc. RNDr. Peter Kodyš, CSc., whom I thank for his help and patience during this work, and for the great and friendly approach throughout the whole study. I would like to thank the whole Czech ATLAS ITk strip collaboration, especially prof. RNDr. Zdeněk Doležal, Dr., RNDr. Jiří Kroll, PhD., Mgr. Martin Sýkora for their suggestion during the study.

I also dedicate this thesis to my family, who supported me throughout my studies and tried to make my studies easier. I also thank my brothers Matej and Jakub, who did not anger me. I also thank my godmother Romana for her huge support, especially during the COVID19 crisis in the last year of study.

Many thanks also to all my friends from Slovakia (2x Tomáš and Vladino) and from Prague (TJ and Ľubo), who always had time to help me clear my head.

The biggest thanks go to Lydia Janitorová (if you read it after 2.1.2021 then Martausová). She makes every day more beautiful, and I really love her.

Title: Tests of Semiconductor Detectors for ATLAS Upgrade

Author: Bc. Marek Martaus

Institute: Institute of particle and nuclear physics

Supervisor: doc. RNDr. Peter Kodyš, CSc., Institute of particle and nuclear physics

Abstract: The semiconductor detectors of ATLAS experiment at CERN are exposed to high radiation for a long time, which reduces their efficiency. They need to be replaced and, if necessary, modernized. Nowadays, the entire Large Hadron Collider is planned to improve. Its luminosity will increase. During this shutdown, the detectors of ATLAS experiment will also be upgraded. This thesis is focused on strip detectors of a new inner detector of ATLAS experiment called ITk.

For the correct interpretation of the measured results, it is important to know the detector's response. Test of detector response is, therefore, an important part of the process of developing. In this thesis, we focused on detectors' edges, where we assumed a different shape of the electric field, which may cause a different response. We chose the laser test because it is a position-sensitive measurement.

Keywords: Characterization of ITk detectors, silicon detector, electronics

Název práce: Testování křemíkových detektorů pro experiment ATLAS Upgrade

Autor: Bc. Marek Martaus

Katedra: Ustav částicové a jaderné fyziky

Vedoucí diplomové práce: doc. RNDr. Peter Kodyš, CSc., Ustav částicové a jaderné fyziky

Abstrakt: Polovodičové detektory experimentu ATLAS v CERNe sú dlhodobo vystavené vysokej radiácií čím sa znižuje ich účinnosť. Je potrebné ich pravidelne vymieňať a prípadne modernizovať. V súčastnosti sa plánuje vylepšenie celého Veľkého hadrónového urýchľovača kedy sa bude zvyšovať jeho luminozita. Počas tejto odstávky prebehne aj modernizácia detektorov experimentu ATLAS. Táto práca je zameraná na stripové detektory nového vnútorného detektoru ATLAS nazývaného ITk.

Pre správnu interpertáciu meraných výsledkov je dôležité poznať odozvu detektora. Testovanie je preto dôležitou súčasťou procesu vývoja nových detektorov. V rámci tejto práce sme sa zamerali na okraje detektorov kde sme predpokladali rozdielny tvar elektrického poľa čím sa môže líšiť aj odozva. Zvolili sme si metódu testovania laserom nakoľko sa jedná o polohovo citlivé meranie.

Klíčová slova: Charakterizační testy ITk detektorů, křemíkový detektor, elektronika

Contents

Introduction

From time immemorial, people have tried to figure out what the world around us is made of. Democritus had already considered the smallest, indivisible part of the matter. It took a long time for people to confirm his theory.

Huge progress has been made with the development of optics and the discovery of lenses and the microscopes. A little more effort was needed to discover the mentioned indivisible parts of matter, atoms. It turned out that the only way to explore such a small world is indirect, through experiments. The idea of the shape of the atom began to form.

Today we know that an atom is not an indivisible and elementary particle. We have confirmed or refuted many theories, discovered new particles, and we use many of them in everyday life. However, we are still not at the end, and therefore it is necessary to modernize the experiments gradually. Planned modernization of the Large Hadron Collider brings us space for the modernization of its detectors, specifically the ATLAS experiment.

To correctly interpret the measured data, it is necessary to correctly understand the functionality and physical processes in particle detection. It is the edges of the detector that are often quite overlooked, but their response may vary.

In this work, we tried to measure the response at the edges of silicon strip detectors. We used a mini version of new types of sensors that will be used in the new Inner Tracker of the ATLAS experiment. We chose laser for its position sensitivity.

In the first chapter, we deal with CERN's description, which also includes ATLAS experiment. Here you will find a brief summary of CERN's history, along with a description of the most significant discoveries. Next, we describe the individual parts of ATLAS as well as the description of the planned ATLAS Upgrade.

The second chapter is devoted to the principle of particle detection, specifically the silicon strip detector. We briefly deal with semiconductors and their use as a particle detector. There is also a mention of signal readout and its processing.

We use various characterization tests to test semiconductor strip detectors. Their description can be found in the third chapter. Individual tests are later used in testing the module.

The fourth chapter describes the layout of the experimental equipment that we used in the measurement. Here you will find a description of the tested detector, the power supplies used and the software needed to perform this measurement. If we use the description in this chapter, it is possible to reproduce the entire measurement.

The response measurement results at the edge of a silicon strip detector are described in the fifth chapter. From the beginning, we focus on individual tests used to set up the whole experiment correctly. Subsequently, all the necessary graphs are summarized here and a description of which part of the detector the given measurement belongs to. An important part is also a simple diagram of the tested module.

The sixth chapter is devoted to the discussion of the measured results. Here we analyze the individual measurements in detail and discuss the differences between

them. We also discuss the accuracy of the measured data and their significance. We also have a few problems during the measurement. These problems are also mentioned in this chapter.

1. CERN

The European Organization for Nuclear Research or CERN (*Conseil Européen pour la Recherche Nucléaire*) is an international organization that focuses on operating laboratory for basic physical research on elementary particles and the structure of matter. There is the largest particle accelerator in the world - LHC (*Large Hadron Collider*) - and other experiments that study particle collisions at the highest energies. The main experiments are ATLAS, ALICE, LHCb and CMS. Their location is shown in figure 1.1.

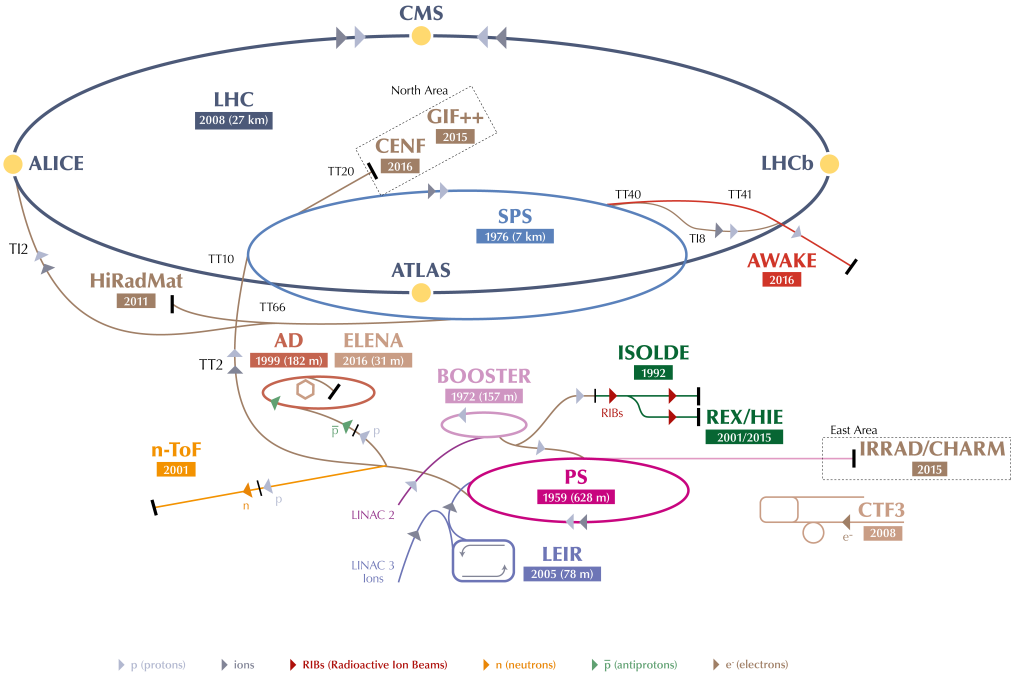

Figure 1.1: Scheme of the CERN accelerator complex. The full names of the individual experiments are given in the list of abbreviations. The years reported for some experiments correspond to their start time, see chapter 1.1. [1]

LHC is circular particle accelerator with a length of 27 km situated in the northwest suburbs of Geneva on the Franco-Swiss border. It consists of two-beam pipes kept in an ultra-high vacuum which intersects in four points. There is also more than 9000 magnets used to direct the beams around the accelerator. It was designed to run at a maximum collision energy of 14 TeV with luminosity $L = 10^{34}\,\mathrm{cm}^{-2}\mathrm{s}^{-1}$ [2].

A Large Ion Collider Experiment or experiment ALICE was build to study the properties of matter at temperatures and densities that were in space only a short time after the Big Bang. The goal is to reconstruct these conditions in the laboratory and examine the mass in a state called quark-gluon plasma.

Large Hadron Collider Beauty or LHCb was build to study the b quark. It helps understand the slight differences between matter and antimatter. Unlike other main experiments, the LHCb uses subdetectors to detect mainly particles thrown forwards by the collision in one direction.

CMS (*Compact Muon Solenoid*) and ATLAS (*A Toroidal LHC ApparatuS*) were both build to study standard model to searching for extra dimensions and new particles. Both use different technical solutions and a different magnet system design.

1.1 History of CERN

CERN was founded in 1954 by the ratification of 12 states. Currently unites 21 member countries including the Czech Republic and Slovakia. CERN's first accelerator, called SynchroCyclotron (SC), was built in 1957. It provided beams for CERN's first experiments in particle and nuclear physics. After 33 years of service, SC was closed down.

Only two years after the launch of SC, the Proton Synchrotron (PS) was launched. It was the world's highest-energy particle accelerator at the time. Super Proton Synchrotron (SPS), first of CERN's giant underground rings, was launched in 1976. Nowadays, SPS operates at up to 450 GeV and has handled many different kinds of particles.

Tunnel for the most significant project, Large Electron Positron collider or LEP, was completed in 1988. A year later, the first injection took place. The accelerator worked for 11 years during which the project documentation of the ATLAS, CMS, ALICE and LHCb experiments were approved. LEP tunnel was used to build the LHC. It was launched in 2008.

During the operation of CERN, several significant discoveries have been made. One of the first was the discovery of weak neutral current using PS and bubble chamber Gargamel in 1973. Weak neutral currents are one way that subatomic particles can interact via the weak force, one of the four fundamental interactions in particle physics. Ten years later, using more powerful SPS, W and Z bosons was detected.

The first antiatom was also formed in CERN. A team led by Walter Oelert created atoms of antihydrogen in 1995 at CERN's Low Energy Antiproton Ring (LEAR) facility. Each one travelled a path of 10 meters with a near speed of light and then annihilated with ordinary matter. In 2011 the ALPHA experiment at CERN trapped antimatter atoms for more than 16 minutes. Charge parity violation was also finally confirmed at CERN in 1999 in experiment NA48 (North Area). This helped explain why there is a matter in the universe despite the existence of antimatter.

One of the last great discoveries is the Higgs boson. It is an elementary particle predicted by a standard model. It was named after Peter Higgs, who in 1964 proposed the Higgs mechanism to explain why particles have mass. It was discovered in 2012 in ATLAS and CMS detectors during collisions at the LHC. In the following years, this discovery was confirmed.

One of the non-physical benefits of CERN is the invention of the web. In 1990 Sir Berners-Lee had written first server software and defined basic web's concept, Http, Html and URL. Originally it was designed as a way for scientists at institutions around the world to share information.

1.2 ATLAS

As mentioned above, ATLAS is one of the main experiments at the LHC at CERN. It is designed in cylindrical coordinates and surrounds one of the interaction points on the LHC. It consists of several subdetectors which are divided into the barrel and end-cap parts. Overall visualization of the ATLAS experiment is shown in figure 1.2.

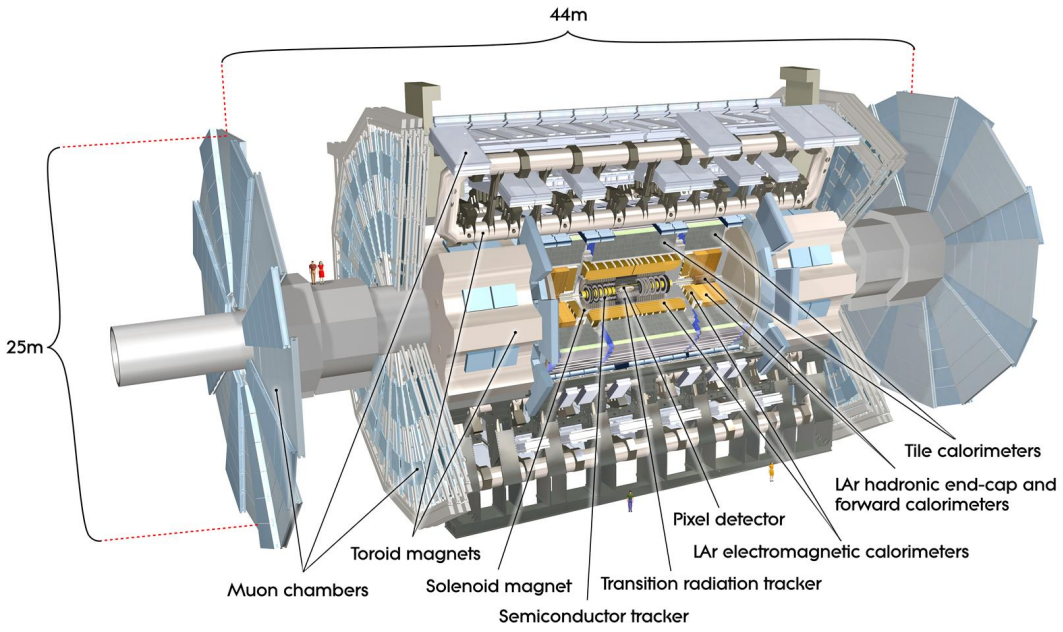

Figure 1.2: Scheme of ATLAS experiment. Its diameter is 25 m and length is 44 m. The weight is around 7 000 tonnes. [3] [4]

From the point of collision, we can divide the detector into an inner detector, a calorimeter and a muon spectrometer. Another important component is the magnetic system, thanks to which it is possible to determine the momentum of the detected particles[1]. Trigger and Data Acquisition System is used to read and process the signal from the detectors.

1.2.1 Inner detector

Inner detector or ID is part of ATLAS experiment. It is located closest to the point of collision. It consists of three different detector systems all situated in the magnetic field to determine the momentum of particle[2]. Scheme of ID is shown in figure 1.3.

The pixel detector is designed to provide very high-precision measurements as close to the interaction point as possible. Due to their placement, they must be highly radiation-resistant. All parameters are set so that short-lived particles can be detected. It consists of three barrel and three end-cap layers on each side.

[1] The magnetic field curves the path of charged particles depending on their momentum.

[2] First two parts are constructed of semiconductor detectors whose principle is explained in the chapter 2.

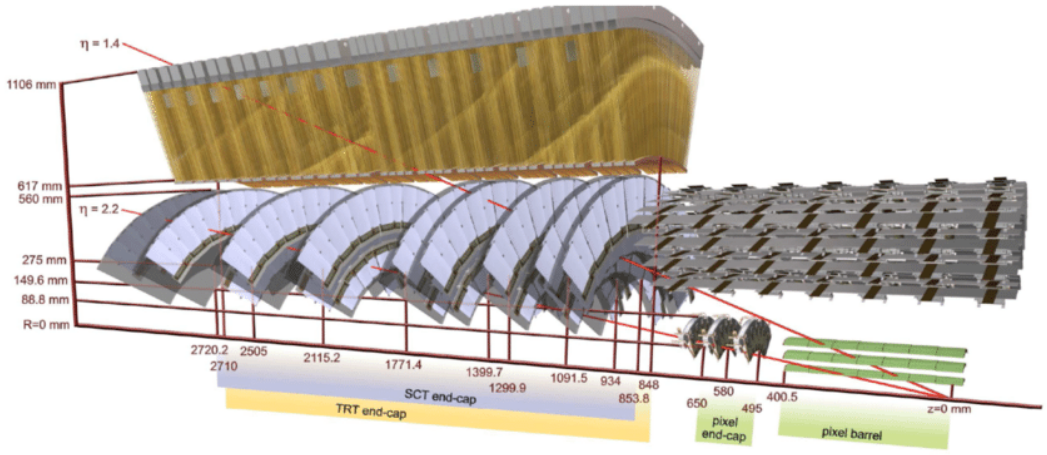

Figure 1.3: Scheme of one-quarter of Inner Detector. The layout of the individual parts is also shown. Barel TRT is not shown. [5]

The area of these detectors is 1,7 m^2 and contains 80 million pixels. Their size is $50 \times 400\,\mu m^2$. [3]

Above the pixel layer, there are silicon strip detectors. This part, together with the pixel detectors, is used to determine the path of the particles and reconstruct the vertex. It consists of 4088 two-sided modules with a total of 6 million read-out strips with a pitch of 80 μm. These modules are divided into 4 barrel and 9 end-cap layers on each side. This makes it possible to determine the position of the particle with an accuracy of 17 μm per layer. [3]

Last part of ID is TRT (*Transition Radiation Tracker*). This part detects transition radiation generated by particles passing through the interface of two media. Its intensity is proportional to the mass and the relativistic gamma coefficient, so TRT provides additional information about the type of particle that has flown through the detector. TRT is the largest part of the ID with a volume of 12 m^3 and consist of 50 000 barrel straws and 250 000 end-cap straws. Each straw is 4 mm in diameter with 0,03 mm gold-plated tungsten wire in the centre. Barrel straws are read-out from both sides, so there are a total of 350 000 read-out channels. The precision of the measurement is 0,17 mm. [3]

1.2.2 Calorimeter

In particle physics, a calorimeter is an experimental device that measures particles energy. It is a block of material in which the energy of the particle is converted into a measurable signal. Through electromagnetic or strong processes interact the incident particle with the detector and produces a shower of secondary particles with progressively degraded energy.

Typically it consists of active and passive layers[3]. Energy deposited in active layers serve as a measurement of the energy of the incident particle. The passive part serves to slow down the high-energy particles and distributes their energy among several secondary particles. By alternating the active and passive layer, a calorimeter is created.

[3]This type is called sampling calorimeter.

Calorimeters can be divided into electromagnetic and hadronic one. Electromagnetic calorimeters is used to measure mainly electrons and photons through their electromagnetic interactions and hadronic calorimeters are used to measure mainly hadrons through their strong and electromagnetic interactions. Instead of semiconductor detector, neutrons and photons can also be detected in the calorimeter.

Both electromagnetic and hadronic calorimeters are used in ATLAS experiment. The active layer of the electromagnetic calorimeter is made of liquid argon, and the passive layer is made of lead. It is called LiAr calorimeter. The passive layer of the hadronic calorimeter is made of steel. The active layer is made of plastic scintillator tiles. The hadronic calorimeter of ATLAS is called TileCal. The distribution of individual types of calorimeters in the ATLAS experiment is shown in figure 1.4.

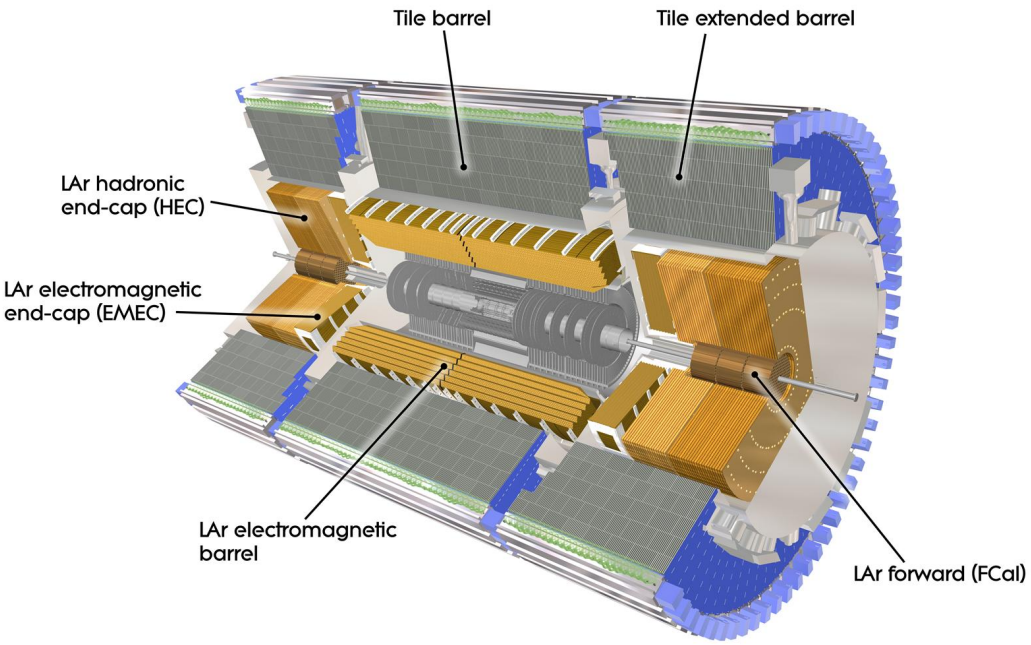

Figure 1.4: Scheme of ATLAS calorimeter. [6]

1.2.3 Muon spectrometer

Muon is lepton that is about 200 times heavier than electrons, so it is much less subject to the Bremsstrahlung effect. The energy loss by ionization is minimal, so it usually passes through the ID and calorimeter undetected. Muon detectors are therefore located furthest from the interaction point.

Accurate measurement of muon trajectories and momentum is an important part of the experiment. Their spectroscopy also contributed to the discovery of the Higgs boson. A very strong magnetic field is needed to measure the momentum of incident muons, so 4 T magnetic field is applied. From the curvature of the muon path, it is also possible to determine the charge of the muon resp. antimuon.

ATLAS muon spectrometer is made of 4 000 individual muon chambers using different detection technologies. The whole system is made of four different subsystems: thin gap chambers, resistive plate chambers, monitored drift tubes, and cathode strip chambers.

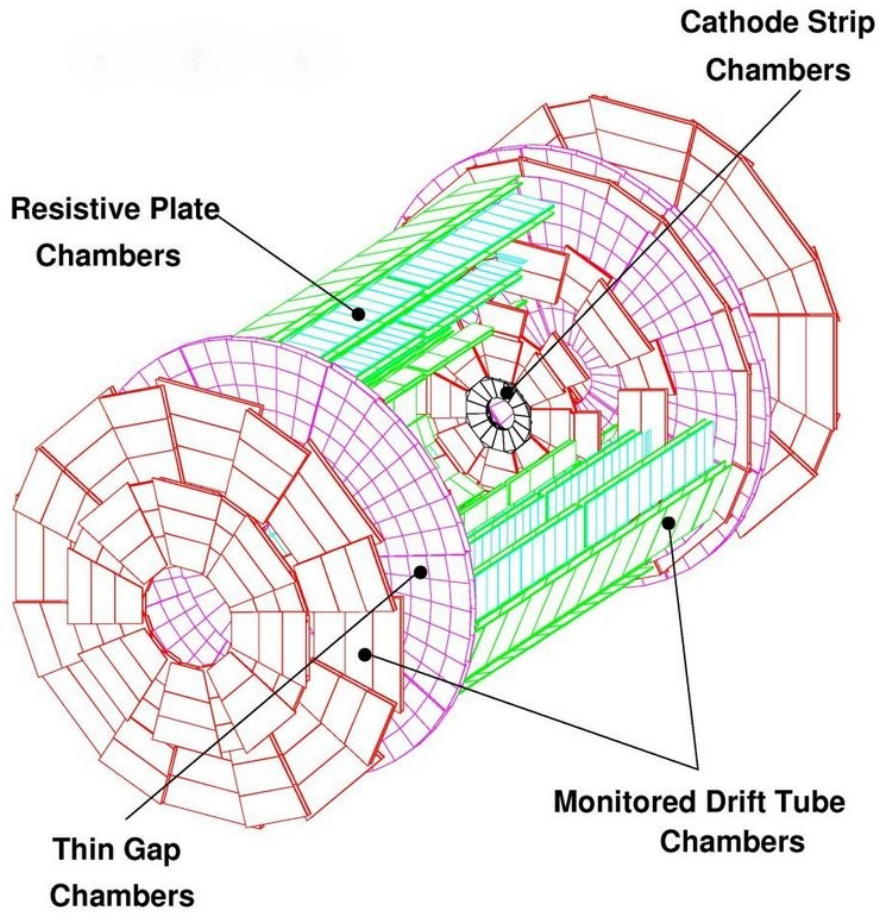

Figure 1.5: Scheme of ATLAS muon spectrometer. [7]

1.3 ATLAS Upgrade

In 2027, it is planned to launch HL-LHC (*High Luminosity Large Hadron Collider*). This is an improvement on the existing LHC to be able to operate with a luminosity of $L = 10^{35}\,\mathrm{cm}^{-2}\mathrm{s}^{-1}$, which is ten times higher than the luminosity of the LHC. Thus, HL-LHC can produce more data. Operation at higher luminosity requires new components to be developed, such as more powerful focusing magnets. Part of the work needs to be done directly in the LHC tunnel. This work will take place mainly during Long Shutdown 3 (2025 – 2027) [8].

The ATLAS detector worked well during its operation. The HL-LHC will collide beams at up to seven times the luminosity for which the ATLAS detector was designed. For this reason, it is necessary to improve the entire detection system. The planned 10-year operation of HL-LHC also requires high radiation resistance of individual components of ATLAS experiment.

The new ATLAS will again consist of three different detector parts. The upgrades will also include a calorimeter and a muon spectrometer, where it is necessary to improve the readout system. In the following text, we will focus mainly on the upgrade of the inner detector. The new inner detector called the Inner Tracker or ITk will only consist of silicon detection modules. Comparison of the layout of the planned ITk and the current ID is shown at figure 1.6.

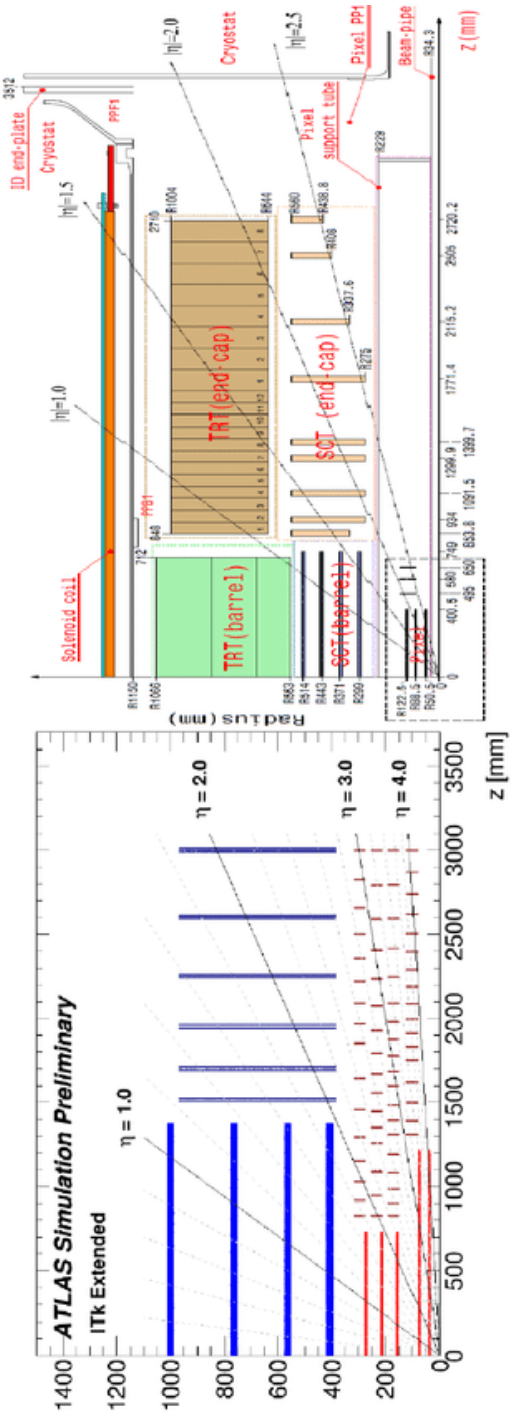

Figure 1.6: Difference in the layout of ID (top) and ITk (bottom). The image is rotated 90° for better visibility. As can be seen, improvements in spatial coverage are planned. For ID, the pseudorapidity was around $\eta = |2{,}5|$ and for the new ITk, the planned spatial coverage is $\eta = |4|$. [9]

As in the ID, the pixel detectors will be closest to the interaction point. They will consist of 5 barrel layers and ring disks as seen in figure 1.6. Two types of pixel sensors should be used in ITk. Planar sensors will be thinner than IDs. Compared to today's 200 μm, its thickness will be $100 - 150\,\mu$m. In contrast, 3D sensors should also be used. These are sensors that not only have a surface structure, but the charge is collected in its entire volume. These sensors show high radiation resistance at low operating voltages.

Silicon strip detectors are also used in ITk instead of TRT. These detectors are divided into four barrel and six end-cap layers. The barrel layers consist of two types of rectangular sensors with a pitch of 75,5 μm and a strip length of 24,1 mm and 48,2 mm. The end-cap layers consist of six different types of trapezoidal sensors. The spacing, in this case, is from 69 μm to 85 μm and the length of the strips ranges from 69,9 mm to 80,7 mm. Together they cover an area of 165 m^2 with over than 6.10^7 read-out channels.

2. Silicon strip detectors

Silicon is a chemical element with the symbol Si, atomic number 14 and it is a member of group 14 in the periodic table. It is a solid-state material which crystallizes in diamond-type latices and belongs to the semiconductors. Each atom has 4 valence electrons through which is covalently bonded to the four nearest neighbours.

After oxygen, silicon is the second most abundant element in the earth's crust. In nature, silicon occurs only in the form of compounds. Chemical methods are currently used to prepare extremely pure silicon. High purity is required for the use of silicon in electronics (and detectors). Typically, a purity above 99,9% is required.

The next step in the processing of extremely pure silicon is the preparation of a monocrystal by controlled melt crystallization called the Czochralski process. In this process, a seed crystal is inserted into the silicon melt. Then it is drawn out by controlled rotation to form a cylinder of pure silicon monocrystal. It is important to control all process parameters, including the melt temperature.

2.1 Band structure

In the case of individual atoms, electrons can only have specific energies given by the solution of the Schrödinger equation. When atoms are grouped into molecules, electrons from different atoms begin to interact with each other and are no longer isolated. For a large number of identical atoms which come together to form a solid, such as a crystal lattice, the atoms' atomic orbitals overlap. Electrons are already very delocalized and interact with each other to form a whole band of allowed energies.

There is always a large number of electron bands in a solid-state material. These bands may overlap each other, or there may be a gap between them where is no allowed electrons energy state, and these gaps are called the forbidden bands. The last electron band occupied by electrons is called the valence band and consists of valence electrons from individual crystal atoms. The first empty electron band is called the conduction band because only electrons that jump to this band contribute to the electrical conduction of the material.

Now, we can classify materials by the width of their forbidden band E_g(as we can see in figure 2.1). Normally, in insulators, the valence band is fully occupied with electrons. Whereas the conduction band is empty. The forbidden band is very large in insulators ($E_g^i \approx 15\,\mathrm{eV}$).

In a conductor, the valence band and the conduction band overlap each other, so there is no forbidden band.

In semiconductors, the forbidden band between the valence band and conduction band is typically about 1 eV. In semiconductors, due to thermal excitation, the electrons enter the conduction band and increase the conductivity. Unlike conductors, the conductivity of semiconductors increases with increasing temperature. For $T \to 0$, the conductivity of the semiconductors is almost zero as expected.

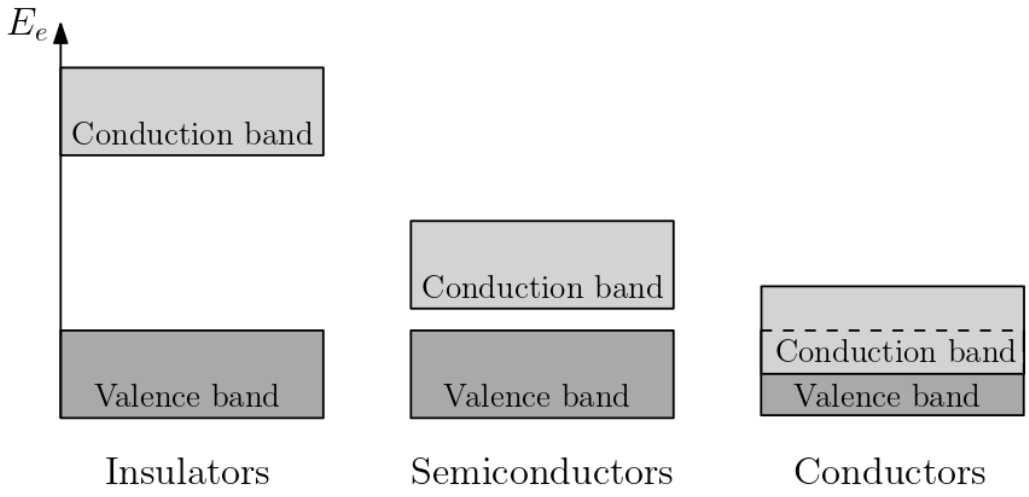

Figure 2.1: Configuration of valence and conduction band for insulators, semiconductors and conductors. E_e is the energy of the electron. Space between two bands for insulator and semiconductor is called a forbidden band or band gap E_g.

2.2 Charge carrier density

As mentioned above, the conductivity in the semiconductor is caused by electrons that have enough energy to cross the forbidden band and jump to the conduction band. The density of these charge carriers is given by equation [10]

$$n = \int_{E_g}^{\infty} D_e(E) f_e(E)\,\mathrm{d}E\ , \tag{2.1}$$

where [10]

$$D_e(E) = \frac{1}{2\pi^2}\left(\frac{2m_e}{\hbar^2}\right)^{\frac{3}{2}}\sqrt{E - E_g} \tag{2.2}$$

is state density at energy E. Here we also use effective electron mass m_e defined as [10]

$$\frac{1}{m_e} = \frac{1}{\hbar^2}\frac{\mathrm{d}^2E}{\mathrm{d}k^2}\ . \tag{2.3}$$

Fermi-Dirac function for fermions is defined as [10]

$$f_e(E) = \frac{1}{\mathrm{e}^{\frac{E-E_F}{kT}} + 1}\ . \tag{2.4}$$

where we use Fermi energy E_F defined as the energy at which the probability of a state is 50%. Using mentioned equations, we get

$$n = 2\left(\frac{m_e kT}{2\pi\hbar^2}\right)^{\frac{3}{2}}\mathrm{e}^{\frac{E_F - E_g}{kT}}. \tag{2.5}$$

If an electron passes into the conduction band, a free space remains. We call this space a hole, and it behaves like a positively charged particle. Analogously for holes, we get

$$p = 2\left(\frac{m_h kT}{2\pi\hbar^2}\right)^{\frac{3}{2}}\mathrm{e}^{\frac{E_F - E_g}{kT}} \tag{2.6}$$

2.3 p-n junction

The use of semiconductors as detectors requires the largest possible area with no free charge carriers, called the depletion region. One option is a semiconductor that does not contain any impurities called an intrinsic semiconductor. For each free electron, there is just one hole, so we get

$$n_i = p_i = \sqrt{n_i p_i} = 2\left(\frac{kT}{2\pi\hbar^2}\right)^{\frac{3}{2}} (m_e m_h)^{\frac{3}{4}} \, \mathrm{e}^{-\frac{E_g}{2kT}} \ . \tag{2.7}$$

The production of intrinsic semiconductors with adequate purity are demanding. The impurities create defects in the lattice, and thus each piece would have different properties such as the width of the forbidden band. A better solution is the controlled addition of impurities called doping. We call it extrinsic semiconductors.

After adding an element with five valence electrons called donor, we get one weakly bounded electron. From an energetic point of view, this electron is located at the upper edge of the forbidden band and thus contributes greatly to the conductivity of the semiconductor. This is called an N-type semiconductor or semiconductor with electron conductivity.

By adding an element with three valence electrons called an acceptor, we get one hole that can be filled by an electron from the conduction band. From an energy point of view, a new energy band is formed just above the valence layer, and thus the conductivity is also increased. In this case, it is hole conductivity, and we call it P-type semiconductors.

The difference between the different types of semiconductors is shown in figure 2.2. In figure 2.3, we can see the position of newly energy bands created by doping.

Charge carriers density in the extrinsic semiconductor is given by [11]

$$n = n_i \mathrm{e}^{\frac{E_F - E_i}{kT}} \ , \qquad p = n_i \mathrm{e}^{\frac{E_i - E_F}{kT}} \tag{2.8}$$

where E_i is the Fermi level of the intrinsic semiconductor and E_F is the Fermi level of extrinsic semiconductor.

Doping does not create a depletion region itself. It is necessary to use both types of semiconductors, especially their connection called PN junction. Because there is a large concentration gradient of both holes and electrons at the junction, the electrons penetrate the P-type semiconductor and recombine with the holes. The free charged particles disappear from the area of a junction, and an electric field generated by the impurity ions appears. Other electrons cannot pass through because of the created electric field. A thin depletion region is created. Using the number of atoms of the impurity N_A and N_D, we can express the internal bias voltage as [11]

$$V_{bi} = \frac{kT}{e} \ln \frac{N_A N_D}{n_i^2}. \tag{2.9}$$

By adding an external voltage V to PN junction with opposite polarity as bias voltage the depletion area expand [1]. We call that a reverse voltage connection.

[1] External voltage V must be higher than internal bias voltage V_{bi}.

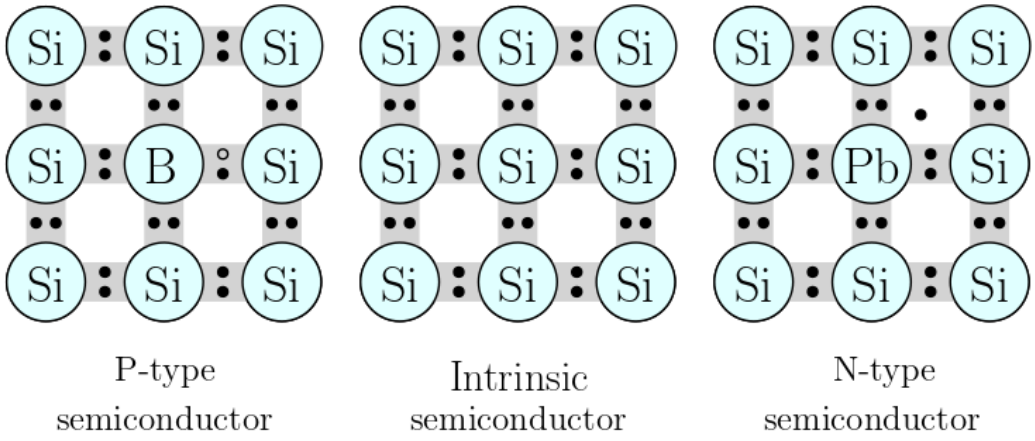

Figure 2.2: Difference between different types of semiconductors. A full black circle shows electrons. Holes are shown by an empty circle. The P-type semiconductor has only three valence electrons, so there is one free hole. The N-type semiconductor has one weakly bounded electron.

For the width of depletion area, we get [12]

$$d = \sqrt{\frac{2\varepsilon}{eN}(V_{bi} + V)} = \sqrt{2\rho\mu\varepsilon(V_{bi} + V)}. \tag{2.10}$$

where N is doping contetration, ε is dielectric constant, ρ is resistivity and μ is charge carrier mobility. Typical values of these parameters for silicon are listed in table 2.1

Table 2.1: Typical values of parameters for silicon[12]

V_{bi}	$\approx$	0,5	V
ε	$\approx$	1	pF/cm
μ_e	$=$	1350	$\mathrm{cm^2\,V^{-1}\,s^{-1}}$
μ_h	$=$	450	$\mathrm{cm^2\,V^{-1}\,s^{-1}}$
ρ	$\approx$	$1 - 10$	$\mathrm{k\Omega\,cm}$

2.4 Silicon as particle detector

Different combinations of PN junctions, typically more than one, are used for particle detection as a sensitive layer. Instead of using p-type or n-type semiconductors, there is a possibility to use p^+, p^-, n^+ or n^-. The index + resp. − is used to indicate a large resp. small concentration of dopants. A typical combination is p^+ and n^- junction.[2] For this configuration, we can write

$$N_A \ll N_D = N. \tag{2.11}$$

[2]Resp. combination of low and high concentration is used to create a wide depletion area. p^- and n^+ can be also used. Especially the same type of semiconductor with different dopant concentrations can be used.

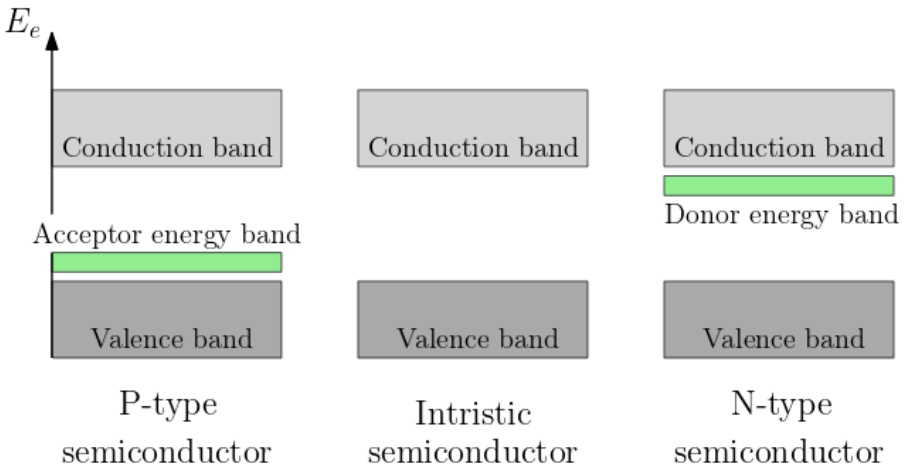

Figure 2.3: Position of a newly created energy band in extrinsic semiconductors. In silicon, the distance of the new energy bands from the edges of the forbidden band is the same. It is approximately $\Delta E \approx 0{,}045\,\mathrm{eV}$ [10].

so we get from eq. (2.10) the relation for depletion voltage [10]

$$V_d = \frac{eNd_{pn}^2}{2\varepsilon} \tag{2.12}$$

where d_{pn} is the width of the sensor.

This junction serves as the sensitive area or sensor. Additional structures are added to construct the whole detector. The most common is the use of a metal-insulator-semiconductor junction. The oxide layer is the typical insulator (e.g. SiO_2), so this structure is called *Metal Oxide Semiconductor* (MOS).

The sensor converts the energy deposited by a particle (or photon) to the electrical signal. In the semiconductor, the absorbed energy is transformed into mobile charge carriers (electron-hole pairs). The number of created electron-hole pairs is proportional to absorbed energy

$$N = \frac{E}{E_i} \tag{2.13}$$

where E_i is mean energy required to produce electron-hole pair. For silicon it is $E_i^{\mathrm{Si}} = 3{,}67\,\mathrm{eV}$[3]. [12] The signal formed in the sensor fluctuates, even for fixed energy absorption. Number of created electron-hole pairs fluctuate statistically so

$$\frac{\Delta E}{E} = \frac{\Delta N}{N} = \frac{\sqrt{FN}}{N} = \sqrt{\frac{FE_i}{E}}. \tag{2.14}$$

where F is Fano factor which comes about because multiple excitation mechanisms can come into play and reduce the overall statistical spread. For silicon, the Fano factor is about $F_{\mathrm{Si}} = 0{,}1$. [12]

The signal pulse shape depends on the geometry of detector which determines the distribution of induced charge. It also depends on the velocity of charge

[3]For minimum ionizing particles (MIP) and 300 μm silicon detector thicknes the most probable charge deposition is about 3,5 fC or 22 000 electrons.

carriers defined as [12]

$$v_i(x) = \mu_i E(x) \tag{2.15}$$

where index i is e for electrons and h for holes. The intensity of the electric field $E(x)$ in the depletion area depends on the applied voltage. If the applied voltage is higher than the depletion voltage, there will be a non-zero field in the entire depletion area. At higher voltages, we can talk about a homogeneous electric field (figure 2.4). The typical configuration of the silicon detector is shown in figure 2.5.

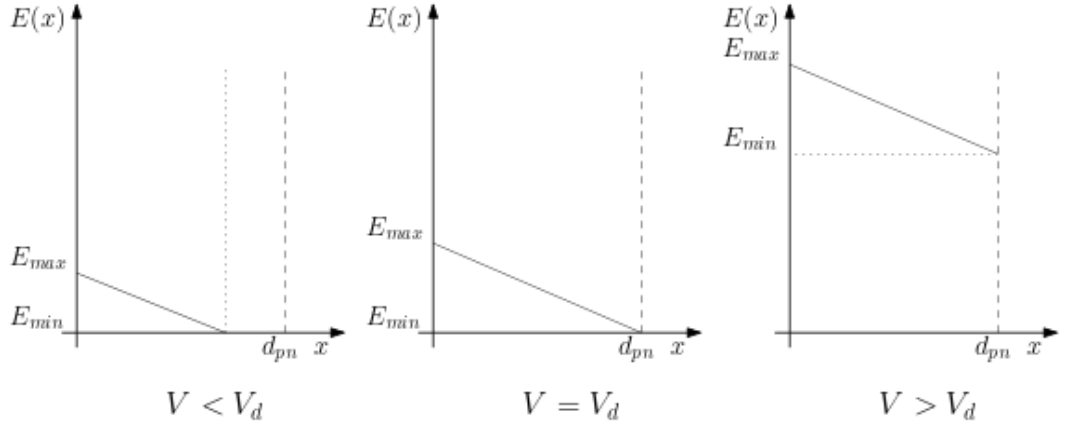

Figure 2.4: Electric intensity in the depletion area for three different external voltages. For $V \gg V_d$, the difference in electric field intensity is negligible, $\Delta E \ll E_{min}$, and therefore we can consider the field to be homogeneous.

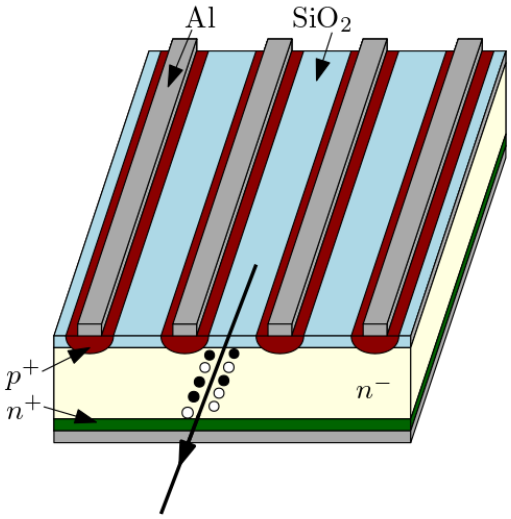

Figure 2.5: Typical configuration of the silicon detector. Incident particle passing through detector creates the electron hole pairs (full black and empty circles). These charge carriers are collected on the electrodes. The upper electrode is segmented into strips to determine the position of the particle. For this case, a resistive charge split is used. A thin resistive layer is applied between the individual strips. The charge created by the incident particle is distributed in proportion to the distances from the individual strips.

2.4.1 Radiation damage

The incident particle does not lose its energy only by ionization. Non-ionizing energy losses cause defects in the semiconductor structure. One of the main defects is the dislocation of lattice atoms. The collision dislocates the atom from the lattice, creating a vacancy and changing the properties of the semiconductor.

Radiation damage affects detection properties. One of the main consequences is an increase in leakage current, which affects the detector noise. It is, therefore, necessary to increase the applied voltage. Furthermore, the charge can be trapped in the vacancies, which causes a decrease in the signal. In the case of a temporary capture, the charge may not be processed in time or be assigned to an incorrect incident.

Radiation damage is not an irreversible process. Depending on the temperature, the damage gradually decreases. This process is called annealing. It is not possible to completely eliminate the damage, but we can significantly reduce it. The damage slowly decreases until it reaches a stable value. Then there is reverse annealing when the damage increases again. The ideal annealing is 80 minutes at a temperature of 60 °C. [10]

2.5 Signal processing

Figure 2.6 illustrates a typical configuration of a detection system. The signal, created in sensor, can be quite small so it is necessary to amplify this signal for further processing. An important factor is electrical noise generated by electrical components. The sensor and preamplifier must be designed carefully to minimize electronic noise.

Another component is the pulse shaper. Its primary function is improving the signal to noise ratio (SN). The frequency spectra of the signal and the noise differ, so we can improve the ratio by adjusting the frequency response so that it gives priority to the signal over noise. It also changes time response resp. pulse shape. Improving SN implies increases the duration of the pulse. We usually measure more than one pulse. Overlapping of individual pulses would lead to large measurement errors. It is, therefore, necessary to set suitable pulse width.

The digitizer converts a continuously varying amplitude into discrete steps using comparators. A more detailed description of the signal processing and the corresponding circuit diagrams is given in [13].

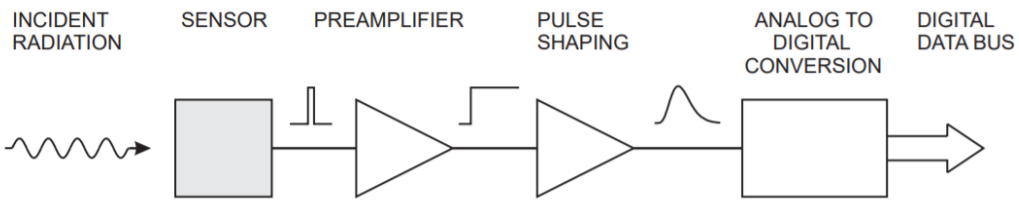

Figure 2.6: Typical detection system configuration.

2.5.1 Readout method

The division of the electrodes into strips provides important information about the position of the particle. It is necessary to read the signal from each strip separately, which is the main limitation on the distance of the strips called pitch. Two different readout methods are used to get the signal from the detector.

The simplest way is a binary readout, which provides us with logical information, whether the signal on a given strip has exceeded the set threshold. Typically, the threshold value is set to three times the noise value. If we assume that the charge is read by one strip, the resolution is given by the relation [10]

$$\sigma_x = \frac{p}{\sqrt{12}} \tag{2.16}$$

where p is a pitch of the detector. If the signal from one particle exceeds the set threshold on several strips, the resolution is about 30% better.

In the case of analogue readout, information about signal amplitude from all strips are stored. In this way, we can also obtain information about the shape of the cloud of charge whose centre of gravity determines the position of the particle. The maximum resolution of this type of readout is about μm. We can also determine the energy deposited in the detector. Due to a large amount of data, the analogue readout is unsuitable for detectors in the ATLAS experiment where binary readout is used.

3. Characterization of silicon detectors

The silicon strip detectors used in the ATLAS experiment must pass a series of tests to demonstrate their functionality and response. Errors can occur during their production and thus some strips may show an incorrect response. These strips need to be detected and marked as dead strips from which the signal is not processed.

Before testing the detectors used in the experiment, prototypes are tested and the response is compared with simulations. During these tests, it is possible to reveal the peculiarities of the newly designed detectors and correctly understand all the physical processes.

3.1 Threshold scan

This is a basic test in which we measure the response of the detector depending on the set threshold. By gradually increasing the threshold, we measure the response, which gives a set of measurements from which we can reproduce the amplitude of the signal. The result of threshold scan is the number of detected signals depending on the threshold for each strip.

If we assumed a delta function signal and neglected the noise, the threshold scan would result in a step function. In reality, the energy of a particle passing through a thin layer of the detector is given by the Landau distribution [14]. If we consider the Gaussian noise distribution, the real signal will be the convolution of the Landau distribution and the Gaussian distribution, also called the Landgauss. The result of the threshold scan is a skewed step function, which can be well approximated by a function which, due to its shape, is also called the S-curve

$$N(x) = \varepsilon_{max}\mathrm{erfc}\left[x\left(1 + 0.6\frac{\mathrm{e}^{-\xi x} - \mathrm{e}^{\xi x}}{\mathrm{e}^{-\xi x} + \mathrm{e}^{\xi x}}\right)\right] \tag{3.1}$$

where $N(x)$ is number of detected hits, ε_{max} is half of S-curve maxima also called vt50 point (*value of threshold at* 50% *maxima*) and ξ is skew factor. The complementary error function contains two other free parameters mean and sigma. By fitting the measured data, we can determine the noise level (sigma) or the value of vt50. We use the vt50 value as a reference value when comparing the response from different strips.

3.2 Response curve

An important part of the detector's characteristics before measuring the response is the response curve. The detector response is given in digitizer units called DAC counts. It is therefore necessary to determine the conversion between DAQ counts and fC. By injecting an internal calibration pulse with a specific charge value, the response in the DAQ count is determined. Specifying this response for multiple values allows you to specify a conversion function.

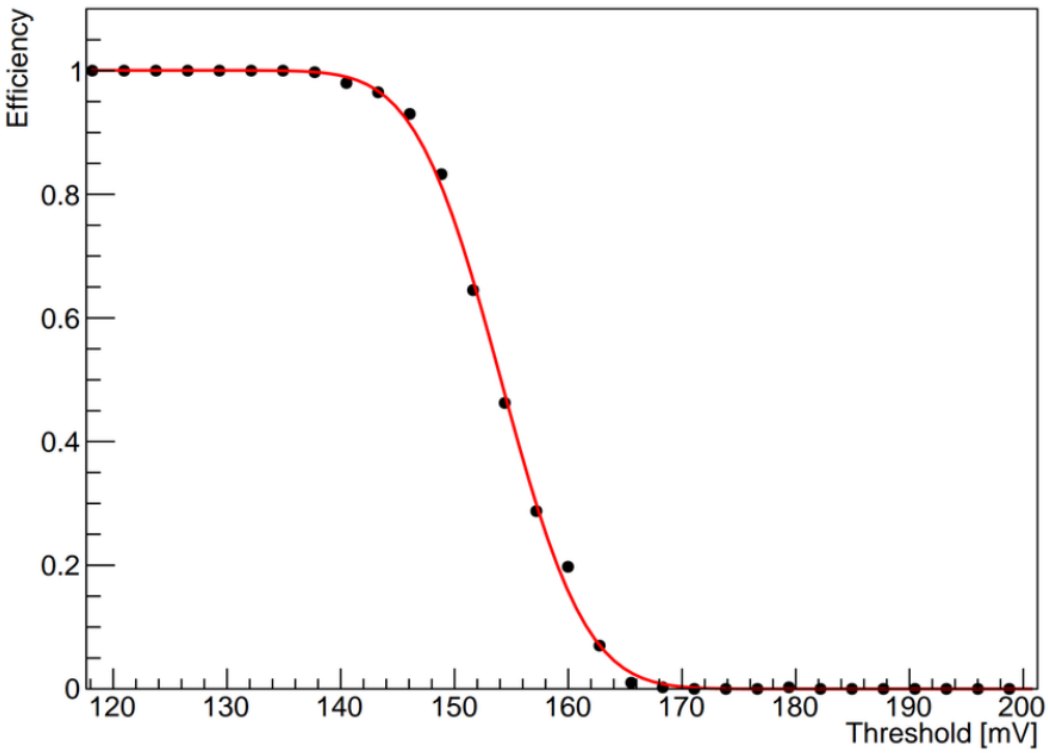

Figure 3.1: Example of threshold scan (black circles) and fitting of measured data by S-curve. The y-axis in this case does not show the number of hits but the efficiency. It expresses the ratio between the number of hits and the maximum number of hits. [15]

In fact, the conversion between DAQ counts and mV is performed first. It is the same for the whole detector and therefore this conversion is often not given. The conversion between mV and fC must be calculated for each readout chip.

3.3 Three point gain

The response curve is not linear. For low values, it can be approximated by a linear function. This is called three point gain (3PG) and is used to quickly measure the response in the case of a low expected signal. As the name suggests, this is a linear fit of the three measured values, typically for calibration pulse charge 0,5 fC, 1 fC and 1,5 fC. The difference between 3PG and RC is shown in fig. 3.2 We can see that a linear approximation is sufficient for a low signal level.

3.4 Strobe delay

A calibration pulse is required to determine the response curve. Before using it, it is necessary to set the correct delay between injecting a calibration pulse and readout. The strobe delay is used to determine the best timing. This value must be set in the configuration file.

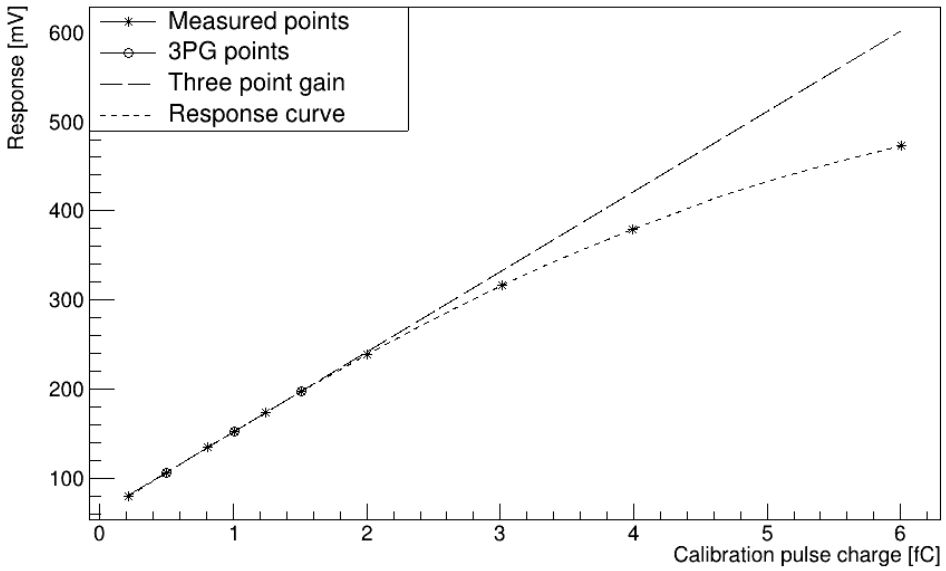

Figure 3.2: Difference between RC and 3PG. To display these curves, data from measurements on a silicon strip detector, which was used in the measurements mentioned in 5, were used.

4. Experimental setup

4.1 Laser test of silicon strip detectors

As part of this diploma thesis, we focused on measuring the response at the edges of silicon strip detectors. This is a position-sensitive measurement, so we decided to use a laser. During laser tests, a laser pulse is applied to the sensitive area of the detector. The laser beam has a well-defined width and is relatively easy to handle, which allows us to aim at a specific part of the sensor.

The specificity of laser measurement is that the laser beam is reflected from metal surfaces. For measurements above the strip, the response is zero. The dependence of the detector response on the laser position has a specific shape, see figure 4.1. In addition to reflection from metallic surfaces, there is also partial reflection at the interface of two environments.

An important part of the measurement is the focusing of the laser on the surface of the detector. We use the reflection from metallic surfaces for this. By finding the two edges of the strip, we can roughly determine its center. By moving the laser in the vertical direction, we determine the points at which we obtain a response even if the laser is located above strip's centre. These are points when the laser spot on the surface of the detector is wider than the strip. We set the laser position to the centre between these two points. By repeating this procedure, we will achieve the required focusing of the laser on the surface of the detector.

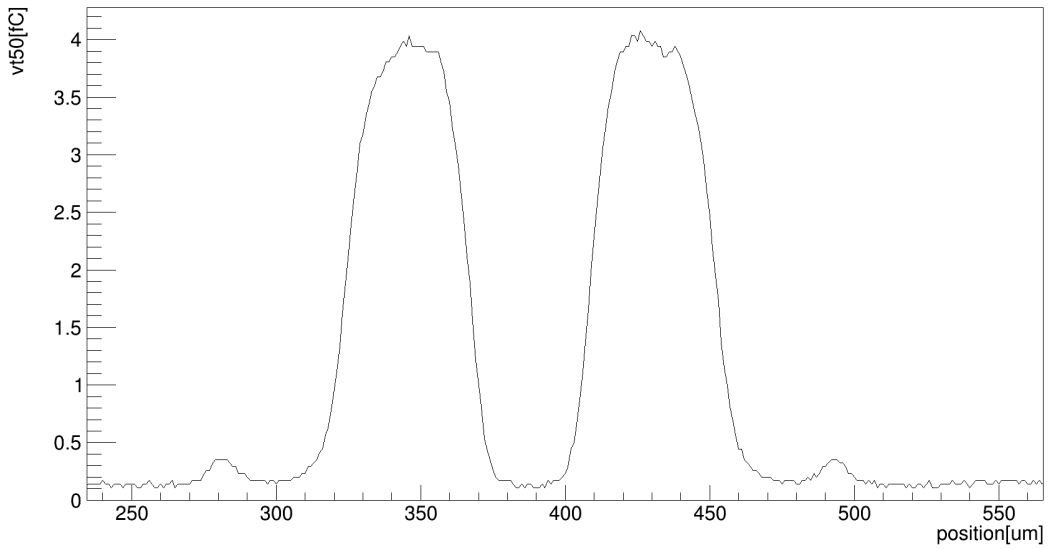

Figure 4.1: Strip 891 response during laser test. The graph shows the decrease in response as it passes over the strip. There are also two small peaks at the point where the response should already be zero. It is caused by reflection of a part of the laser beam from the edge of adjacent strips.

4.2 Experimental setup

The measurement was performed in Clean Room 1 (CR1). It is located in the Institute of Particle and Nuclear Physics (IPNP) laboratory in Prague. The experimental setup is shown in figure 4.2.

The test module, laser and translation stages are placed in a black box (see figure 4.3) to prevent noise caused by room lighting. The arrangement of these parts in the black box is shown in figure 4.4.

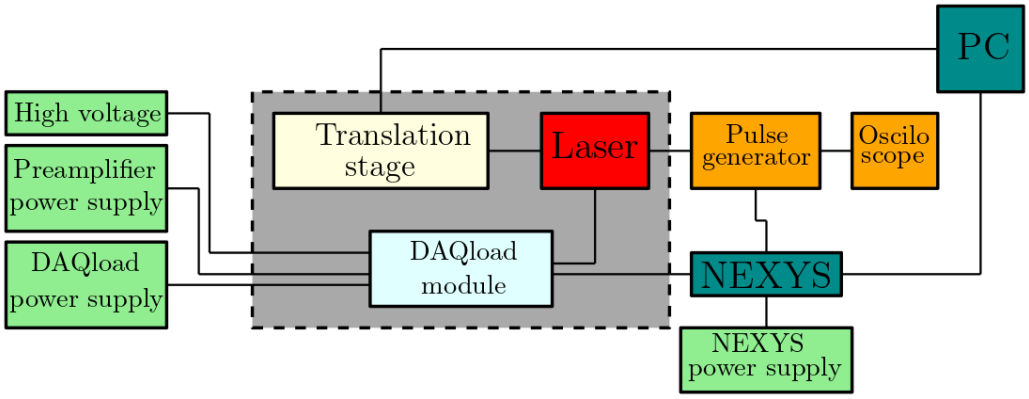

Figure 4.2: Scheme of experimental setup used for measurements.

Figure 4.3: Black box used in the measurement to prevent the access of light from the room which would cause high noise.

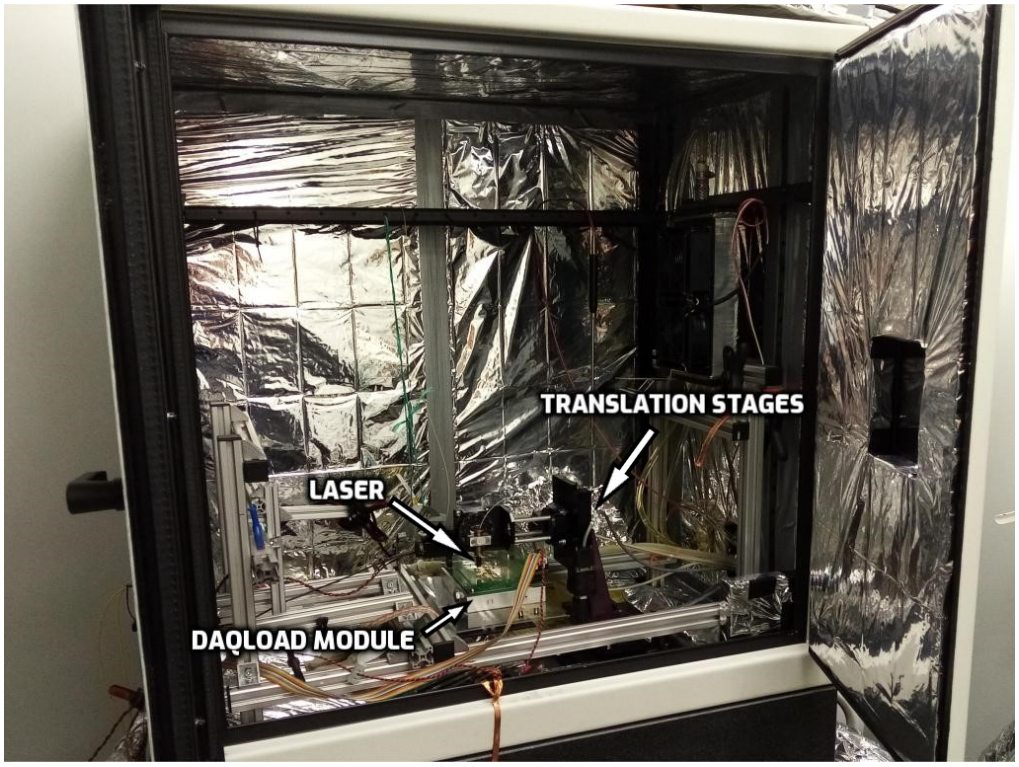

Figure 4.4: Open Black box with the layout of the experimental devices.

4.2.1 Tested module and readout

To measure the edge effects on silicon strip detector, we chose the endcap module DAQload. In figure 4.5 we can see this module located in the test frame which ensures the connection of the necessary electronics for testing in the laboratory. This module consists of a reading chip ABC130 which is bonded to the ATLAS12A mini sensor[1]. This sensor with a thickness of 320 μm has 128 strips[2] with a pitch about 65 μm. The sensor is shown in figure 5.3.

Communication between the detector and the computer is provided by the NEXYS Video card. Using a program called Digilent Adept, it is necessary to upload corresponding firmware. For this measurement, we used the firmware version `nexysv_itsdaq_vb19b_FIB_STD_H`.

We use ITSDAQ software version 4635 to readout the signal. Its use is possible on computers with Windows or Linux operating systems with corresponding version of MSVC [16] and ROOT [17][3] installed. Using ITSDAQ software, it is possible to perform all the necessary basic tests and characteristics of the detector as well as to run your own macros necessary for the measurement. In our case, we used a macro that controls the movement of the tables, readout and store data and plot them in a basic graphs. This graphs are used to evaluate the accuracy of the measurements.

[1]ATLAS12 is one of the new sensors created for ITk. Two different types will be used ATLAS12A and ATLAS12M. The difference between them is in the distribution of the strips. Mini versions are created from the same silicon wafer as the main sensors.

[2]There is also one mini additional strip.

[3]ROOT is a framework that uses a set of libraries written in C ++ used to process and plot data, especially in particle physics.

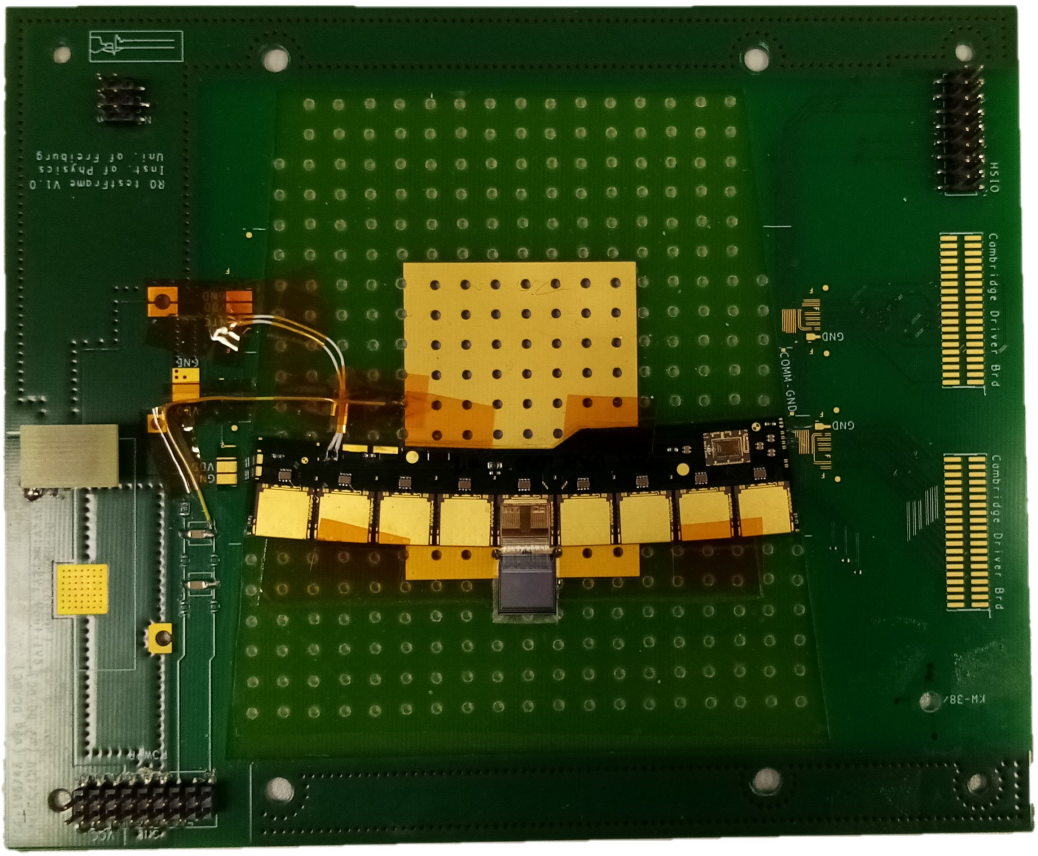

Figure 4.5: Tested DAQload module connected to the test frame. It can be seen from the picture that only the middle chip is connected. The tested ATLAS12A mini sensor can be seen under the chip.

4.2.2 Movement

The accuracy of the measurement is significantly affected by the accuracy of the laser movement. To do this, we used STANDA 8MT167-100DCE2 translation stages that can ensure movement with a minimum step of 0,2 μm[18]. The manufacturer states an error of 0,023 μm[18]. These tables are controlled via a computer using the STANDA 8SMC5 controllers. For movement in three directions, we used three translation stages that were perpendicular to each other. All necessary information about individual translation stages and their control via computer is written in table 4.1.

Table 4.1: Translation stages connection info

direction	positive direction	USB port	Controller ID
horizontal	up	COM6	3151
perpendicular to strips	back	COM5	3216
parallel to strips	left	COM4	649

It is also necessary to ensure a suitable rotation of the laser relative to the tested detector. If the laser beam fell at a large angle, we would not be able to represent the measured data correctly. Therefore, the laser is still mounted on the swivel arm.

4.2.3 Laser

Another major part of the measurement is the laser. We chose a semiconductor infrared laser with a wavelength of 1060 nm. An optical fibre guides the generated laser pulse to the black box. In it, the beam is focused with the help of lenses.

For lower laser intensity, the laser beam is incoherent and unstable. For higher intensity, we get a high response, which can cause damage to the detector. It is necessary to set this intensity appropriately.

4.2.4 Power supplies

For the detector's correct functionality and the NEXYS Video card, it is necessary to set the correct value of the electrical voltage at the input. For this, we used a low voltage source TTi CPX400SP (see figure 4.6) which has an output voltage resolution of 10 mV (see [19]). Due to the very sensitive electronics, it is necessary to check the correct value of the input voltage. Same low voltage sources are used as detector power supply. It is necessary to power the readout chip and preamplifier. The required voltage values are written in table 4.2.

As mentioned in chapter 2, it is necessary to create an depleted area by applying an depletion voltage. We used a Keithley 2410 (see figure 4.6) high voltage source for this purpose. We chose a depletion voltage of −200 V. The sign is important in this case, but it depends on the detector's specific connection to the high voltage source. Before the first measurement, it is therefore necessary to test by applying a small voltage, whether the current through the detector does not increase significantly. The value of the depletion voltage must also be set gradually in steps of about 10 V.

Table 4.2: Power supplies set voltage

NEXYS video	**Preamplifier**	**Readout chip**	**Depletion voltage**
12 V	1,55 V	4,5 V	−200 V

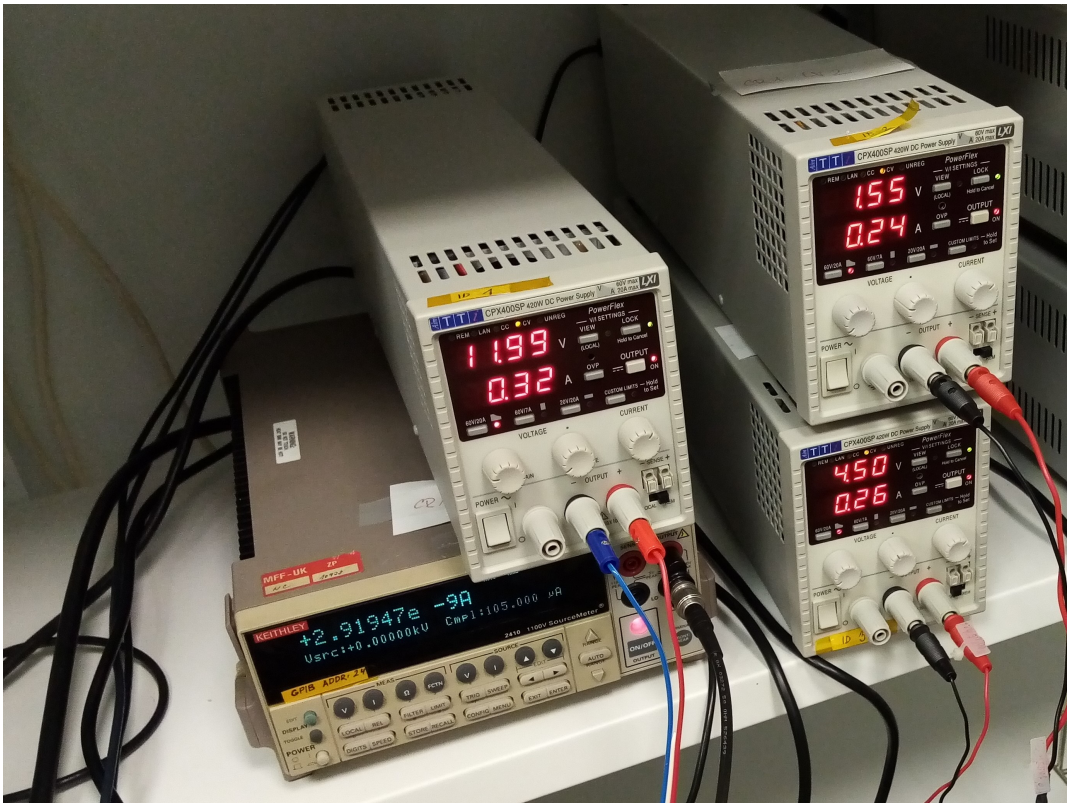

Figure 4.6: Arrangement of power supplies. We can see TTi (top and bottom right) and Keithley (bottom left).

5. Results

5.1 Strip numbering

Before processing the results, we will introduce a convention according to which we will label the individual strips. The sensor contains 127 bonded strips which are connected to one of the readout chips[1]. The readout channels correspond to the individual strips. In our case, the individual strips correspond to the readout channels number 769 - 895.

If we had more sensors connected, the numbering of the strips according to their number, would be confusing. In the following text, the individual strips will be marked according to the number of the readout channel to which they are connected. In a real experiment, we also get information about the readout channel from which the signal was read.

5.2 Laser parameters

Before measuring the edge effects on the sensor, it is necessary to set the laser parameters correctly. The individual parameters can influence each other, and therefore it was necessary to perform multiple measurements and gradually fine-tune the laser parameter values. The final parameter's value was set according to the last measurement with the other parameters set correctly.

Main parameters of the laser pulse are written in table 5.1. Laser pulse delay and laser intensity are given by measurements which are described in the following subsections. Laser width is set to the lowest possible value to avoid not collected free charge carriers.

Table 5.1: Parameter of laser pulse

Laser pulse delay	36	ns
Laser intensity	2,02	V
Laser pulse width	10	ns

5.2.1 Laser pulse delay

Laser pulse delay is a special value that plays a role only in laser tests. If the signal is not collected, it gradually decreases. It is necessary to set the correct timing between the generation of the laser pulse and the detector's readout.

Figure 5.1 shows three peaks. The distance between the individual maxima is approximately 25 ns, which is exactly the time of one time-bin in which the signal is read. In our case, we read three consecutive time-bins. If the signal is injected between these time-bins, it is divided. This can be seen from the decrease in response between peaks. The maxima correspond to the middle of the individual time bins, and it is best to set the delay to the middle maximum.

[1]There are also 2 unassembled strips on the sensor, which are indirectly connected to the adjacent strips.

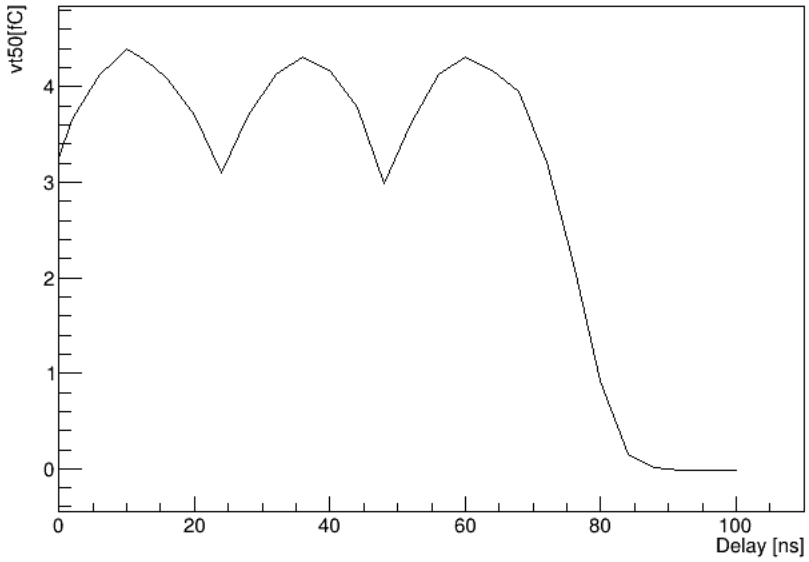

Figure 5.1: Dependence of the vt50 point on the laser pulse delay. The measurement was done approximately 25 μm from strip 782. The laser delay was set to 36 ns for further measurement.

5.2.2 Laser intensity

It is necessary to adjust the laser intensity to achieve the required response. Since the response curve is not linear, this dependence is not linear either. High-intensity values could damage the detector. However, we no longer know the exact shape of the response curve for these values, so these values might not be determined correctly.

5.3 Laser test

Before measuring the edge effects on the silicon strip detector, we checked the edges of the sensor, thus defining interesting places where it would be appropriate to perform the measurement. We marked the edges of sensor A and B as can be seen in figure 5.3. Both edges contain strips of different lengths due to the geometry of the sensor. Thus it is possible to examine the responses from the same strip at the point where it is on edge and at the point where it is second in order. A diagram of the edges of the sensor is shown in figure 5.4. All important parts and strips that were important in this measurement are also shown here.

By moving the laser beam over the examined area, we measured the dependence of the detector response[2] on the laser position. We performed the measurement every 0,5 μm. We tried to automate the whole measurement process as much as possible.

[2]Represented by point vt50.

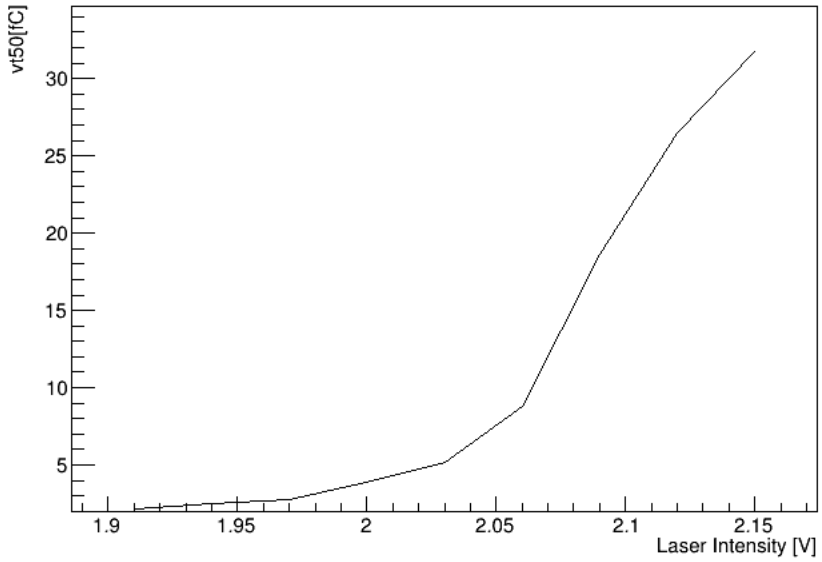

Figure 5.2: Dependence of the point vt50 on the intensity of the laser beam. The measurement was done approximately 20 μm from strip 888. The laser intensity was set to 2,02 V for further measurement.

Part A

On this region there are two shortened strips number 895 (shorter one) and 894, which we focused on when measuring the edge effects. We performed two measurements for both edge strip options. The results are shown in figure 5.5 and 5.6.

As can be seen in figure 5.7, each strip is terminated by a bond pad for connecting the strip to the measuring instrument. It is a measurement of various electrical characteristics, such as interstrip capacity, interstrip resistance, etc. Also, there is a visible internal structure by which the strips are connected to the guard ring which serves to improve breakdown voltage and reduce leakage current of silicon detectors.

We also performed measurements over these structures. Figure 5.8 shows a measurement above the bond pad of strip 894 and figure 5.9 shows a measurement above the internal structure by which strip 894 is connected to the guard ring.

Part B

In part B there are two shortened strips number 767 (shorter one) and 768, which are not connected directly to the readout electronics on the upper side like the other strips. The signal from these strips is read through strips 770 and 771 to which they are conductively connected. This connection can be seen in figure 5.10.

The measurement took place in two places. First, we measured the response at the point where the edge strip is directly connected to the readout electronics. This measurement is shown in figure 5.11.

At the point where there is a strip 768 on edge, which is not directly connected

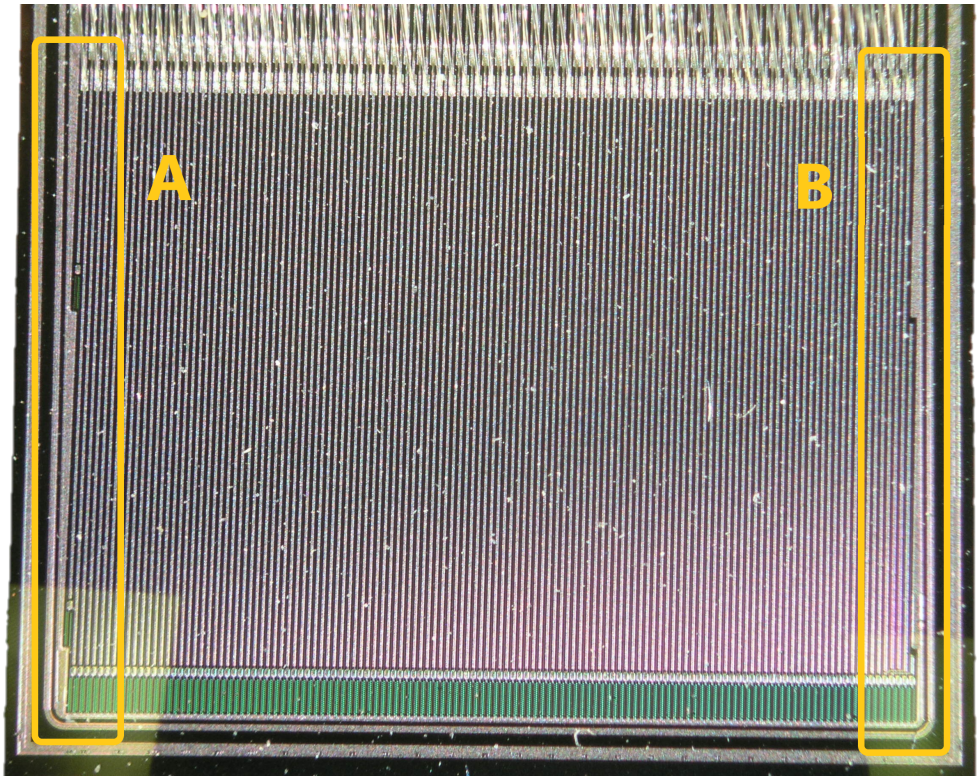

Figure 5.3: Detail of the used sensor with marking of the edges on which we performed the measurement.

to the reading electronics, we performed a second measurement. The number of the strips in the graphs corresponds to the number of the readout channel, and therefore the signal from strip 768 is assigned to strip 771. This measurement is shown in figure 5.12.

Table 5.2 lists information on all the mentioned response measurements at the edges of the detector.

Table 5.2: Informations about response measurments

	Edge strip number	**Figure number**	**Note**
Part A	895	5.5	
	894	5.6	
	894	5.8	*Above bondpad*
	894	5.9	*Above internal structure*
Part B	769	5.11	
	768	5.12	*Unbounded strip*

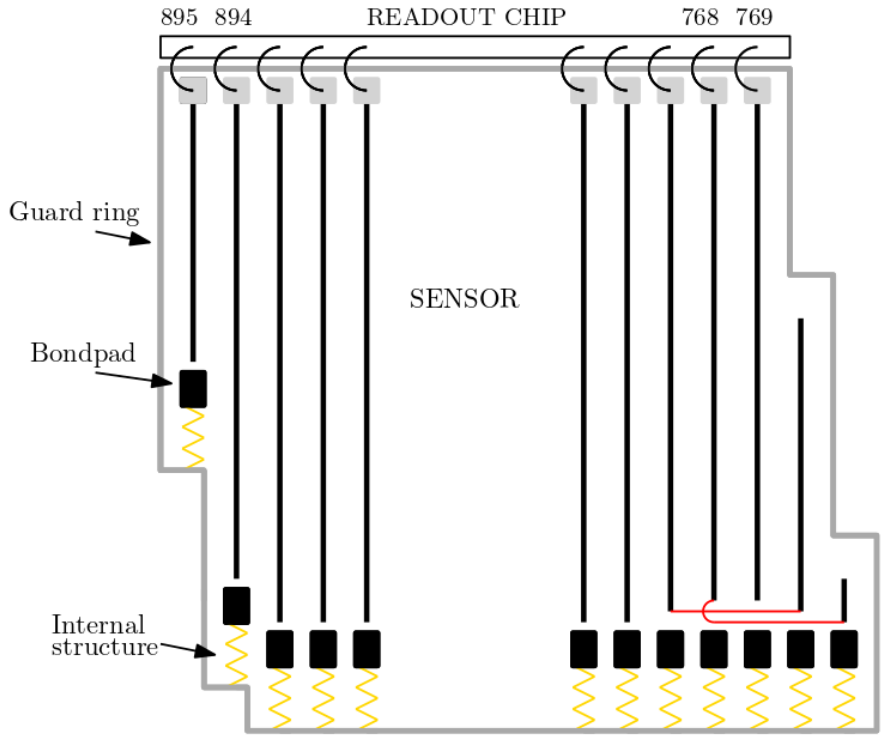

Figure 5.4: Drawing of the sensor with marked tested strips and other important structures. The numbers of the edge read channels are marked above the strips. The figure also shows the connection of unassembled strips to adjacent strips.

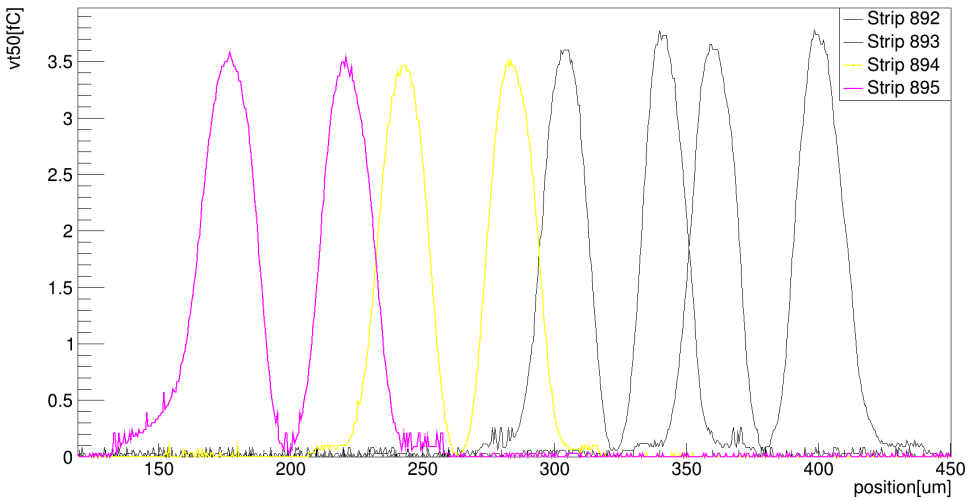

Figure 5.5: Dependence of the detector response on the position of the laser beam for the edge strip number 895.

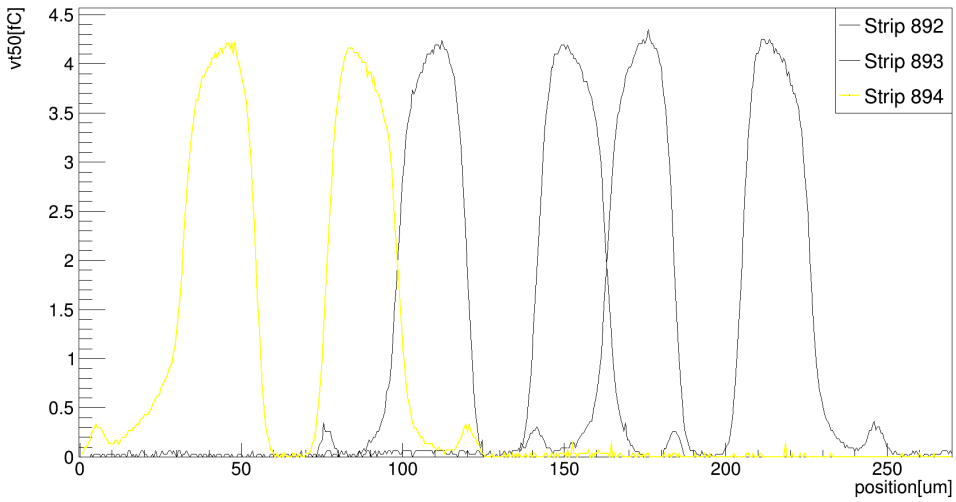

Figure 5.6: Dependence of the detector response on the position of the laser beam for the edge strip number 894.

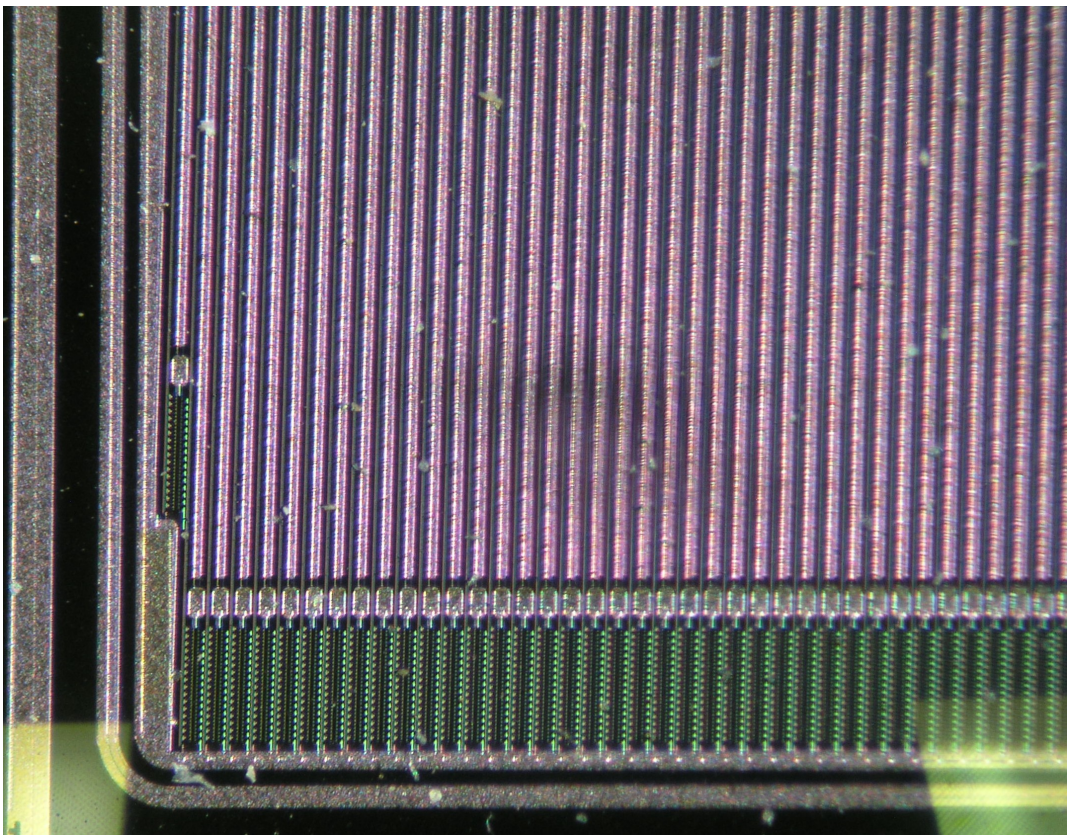

Figure 5.7: Detailed view of the bottom of part A. Here we can see bond pads and the connection of individual strips to the guard ring.

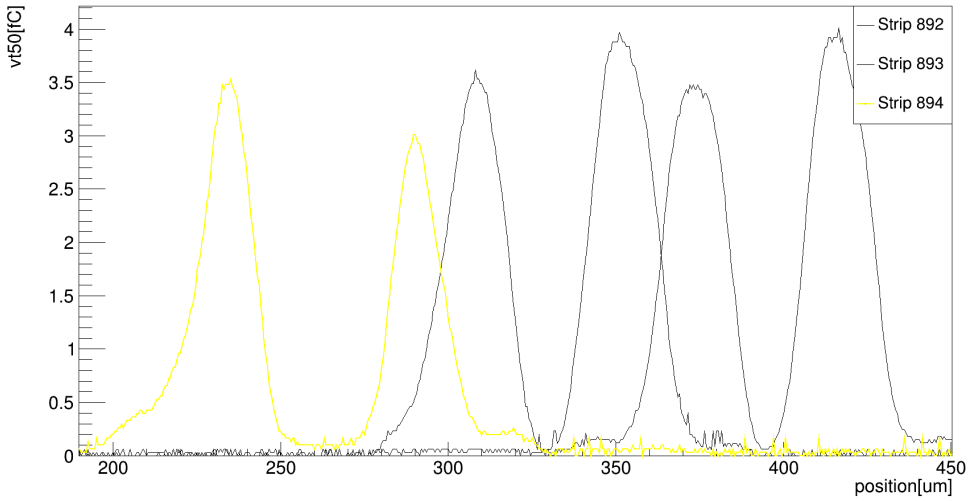

Figure 5.8: Dependence of the detector response on the position of the laser beam for the edge strip number 894. Measurement above the bond pad

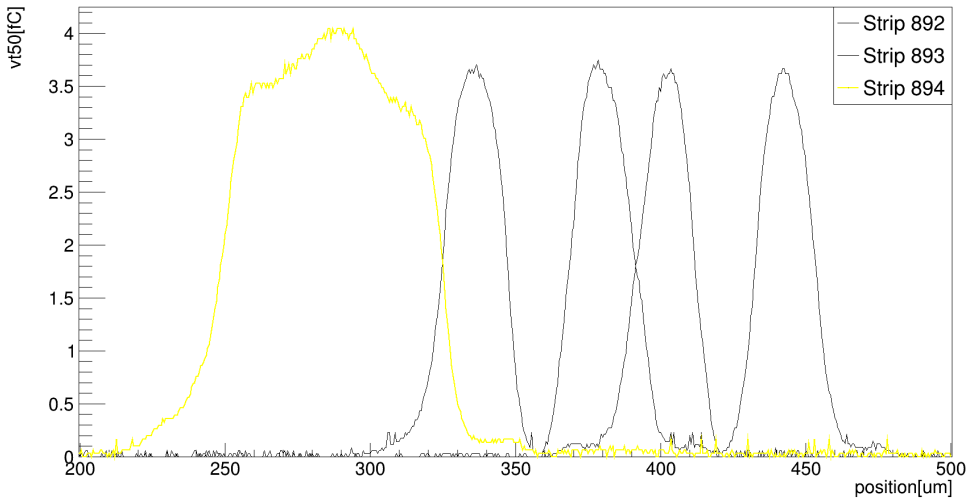

Figure 5.9: Dependence of the detector response on the position of the laser beam for the edge strip number 894. Measurement over the internal structure by which the strips are connected to the guard ring.

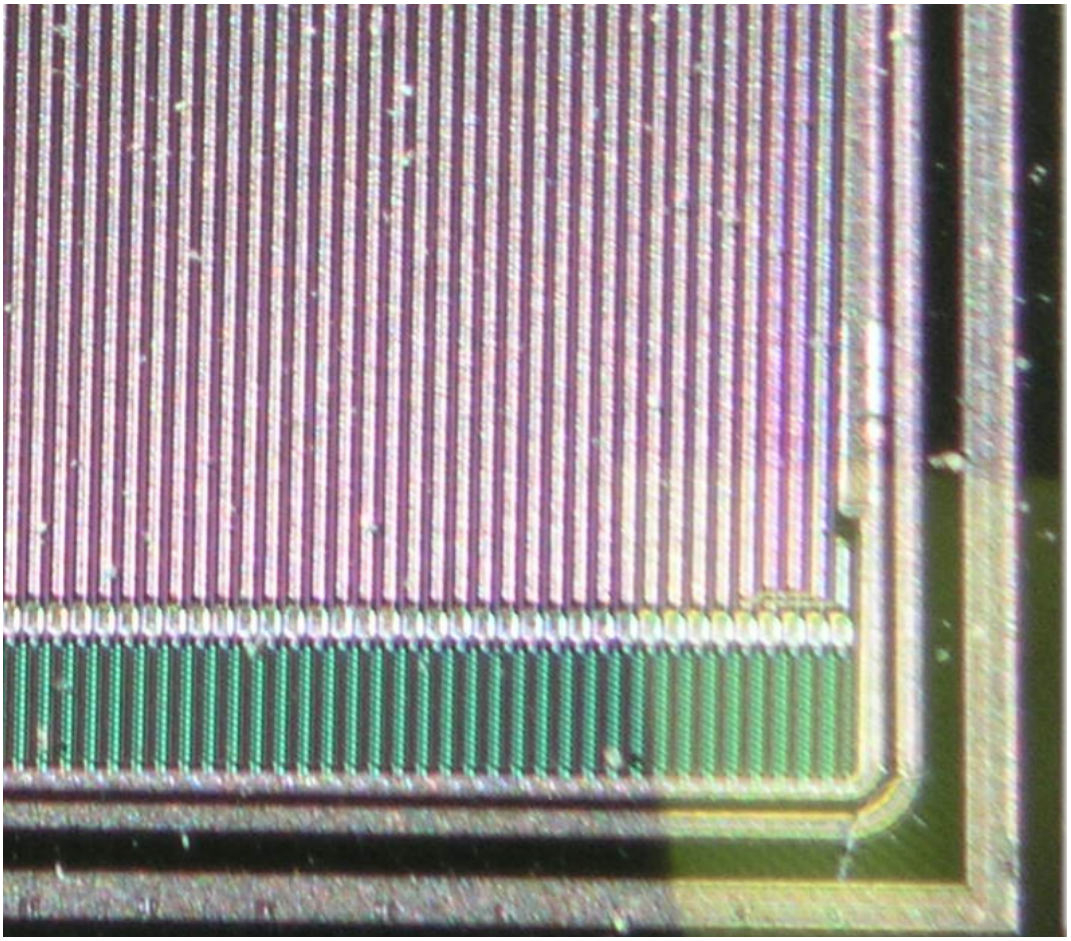

Figure 5.10: Detailed view of the bottom of part B. Here we can see the connection of unconnected strips so that it is possible to read the signal from them.

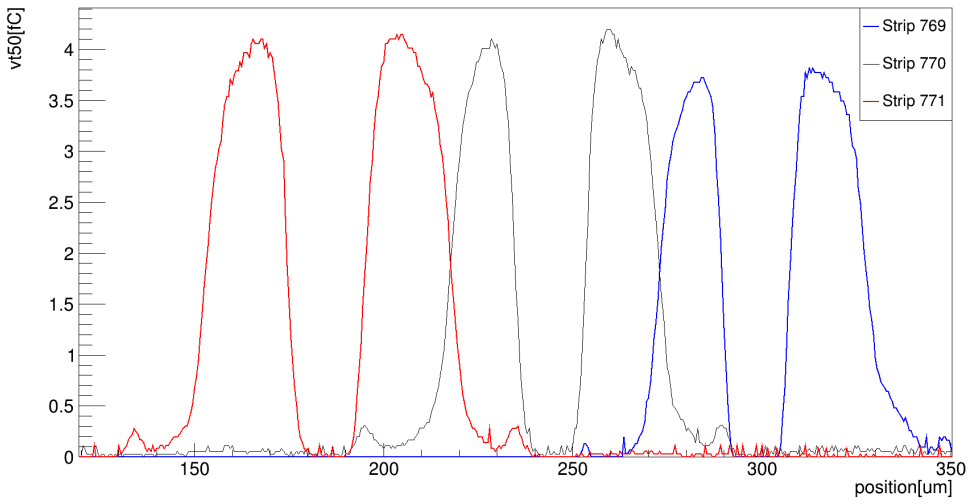

Figure 5.11: Dependence of the detector response on the position of the laser beam for the edge strip number 769.

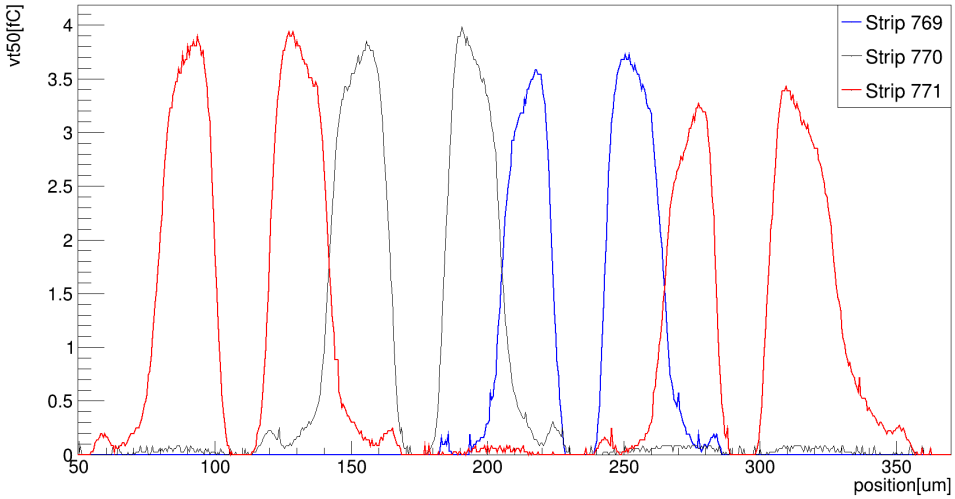

Figure 5.12: Dependence of the detector response on the position of the laser beam for the extreme strip number 768. This strip is not directly connected to the readout electronics and is connected indirectly to channel number 771.

6. Discusion

6.1 Problems

While measuring the edge effects on a silicon strip detector, we encountered a few problems related to the accuracy of the measurement. As mentioned in chapter 4, the measurement took place in CR1. It is a laboratory with controlled temperature and air filtration. However, due to an electrical problem, it was necessary to turn off both the air conditioning and air filtration. Thus, the temperature during the measurement was not constant.

To determine the influence of external factors on the measurement, we performed a stability test. For approximately 17 hours, we measured the response every minute at the same location. The result is shown in figure 6.1.

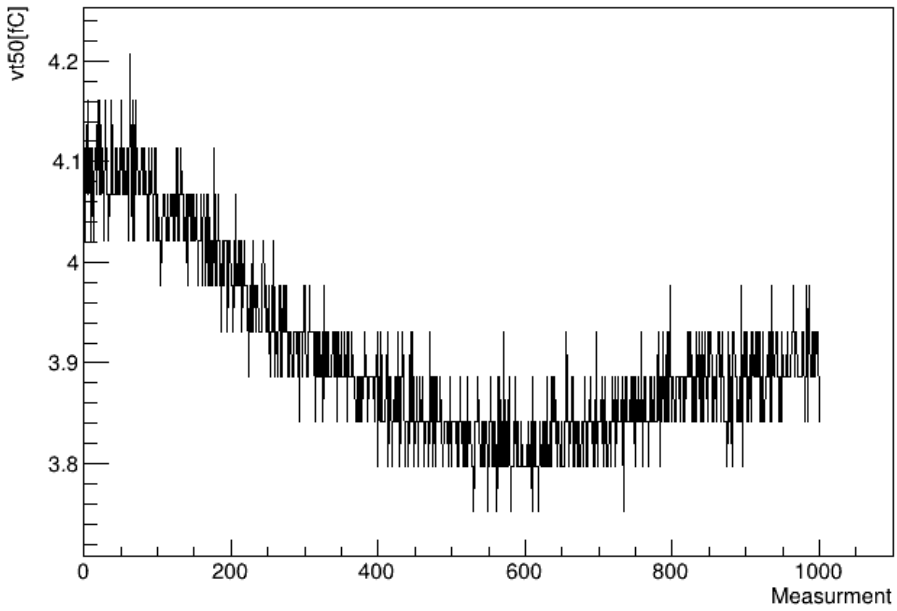

Figure 6.1: Stability test of the measurment. Every minute we performed the measurement in the same place. This measurement directly indicates a measurement error.

It can be seen from the figure that the measurement deviations are quite significant within the whole tested section. The individual measurements take place over a shorter period of time (approximately 4 hours). We are also interested only in a qualitative comparison of the response of individual strips. Therefore, we are only interested in local fluctuations, which are significantly lower.

Another problem we encountered during the measurement was the stability of the electrical network. It often happened to us that the measurement switched off. We found that this happened during working days when fluctuations in the electricity network could occur due to high consumption.The fine readout electronics are sensitive to these fluctuations. We were forced to measure only during the night or on weekends.

6.2 Discusion of edge effect measurments

It is clear from the graphs in chapter 5 that the response of the end strip differs from the response of the strip located between the other two strips. The main difference is the shape of the leading edge of the response for one strip. As the charge is collected even at a greater distance from the strip, the leading edge is milder for the edge strip.

This effect is most visible in figure 5.5 and figure 5.6. In these graphs, we can compare the response of the same strip 894 in two different positions. In graph 5.5 it is located between the two strips and in graph 5.6 it is located at the edge of the sensor. As mentioned above, comparing two measurements is difficult as the measurement is highly influenced by external effects. Qualitatively, the difference in response is observable.

For strip 894, we were also able to measure the edge effects in places of the bond pad (see figure 5.8) or in places outside the metal structure (see figure 5.9) where there was no reflection of the laser beam. In both cases, the edge effect is not so visible as in measurements mentioned above, mainly due to the poorer focusing of the laser beam. As it is necessary to hit a small area during this measurement, better focusing is difficult. In figure 5.9, we see that the response at the place where the reflection of the laser beam usually occurs is higher. This can be caused by the internal structure of the place above which we pass. The formation of free charge carriers also depends on the material.

A comparison of the response in the edge and non-edge strip can also be made by examining the graphs in figure 5.11 and figure 5.12. For strip 769, we see a difference in response, whether it is at the edge or not.

An important finding is that we get feedback from unbonded strips. In figure 5.12 we can see that the response from the channel 771 is also obtained from the places where the unbonded strip is located. As mentioned above, this is a conductive connection of the unbonded strip and the loaded strip.

Silicon semiconductor detectors can contain many different edge structures. Information about them must be well known before the experiment itself. Otherwise, the measurement results may be misinterpreted.

Conclusion

This work was focused on laser tests of silicon strip detectors. The principle of these detectors and their use in large experiments is written in the first two chapters.

The main benefit of this work is the determination of the response at the edges of silicon strip detectors. The experimental setup together with the measurement results is also part of this work. The last chapter discusses the individual results.

The results of this work agree with expectations, which we determined before the measurement. We measured the response at the edges of the silicon strip detectors and found that it differed qualitatively from the response in the centre of the sensor.

Bibliography

[1] The CERN accelerator complex. http://cds.cern.ch/record/2197559. [cited 2020-20-06].

[2] LHC info. https://www.lhc-closer.es/taking_a_closer_look_at_lhc/1.lhc_parameters. [cited 2020-20-06].

[3] ATLAS fact sheed. https://cds.cern.ch/record/1457044/files/ATLAS%20fact%20sheet.pdf. [cited 2020-20-06].

[4] ATLAS info. https://atlas.cern/discover/detector. [cited 2020-20-06].

[5] Lucia Masetti. Atlas inner detector: Commissioning with cosmics data. *European Physical Society Europhysics Conference on High Energy Physics*, 03 2010.

[6] Calorimeter visualization. https://cds.cern.ch/record/1095927. [cited 2020-20-06].

[7] Nir Amram and Erez Etzion. Hough transform track reconstruction in the cathode strip chambers in atlas. 07 2020.

[8] HL-LHC new schedule. https://home.cern/news/news/accelerators/new-schedule-lhc-and-its-successor. [cited 2020-25-06].

[9] Ryan Atkin. A characterisation of the atlas itk high rapidity modules in allpix and eutelescope. *Journal of Physics: Conference Series*, 889:012017, 09 2017.

[10] Z. Doležal. Polovodičové detektory v jaderné a subjaderné fyzice. http://ipnp.cz/~dolezal/teach/semicon/semi_p.pdf. [cited 2020-06-06].

[11] G. Lutz. *Semiconductor Radiation Detectors*. Springer, Berlin, 1999.

[12] C. Patrignani et al. Review of Particle Physics (Particle Data Group). *Chin. Phys. C*, 40:100001, Oct 2016.

[13] H. Spieler. *Semiconductor Detector Systems*. 1 edition. Oxford University Press, 2005.

[14] Z. Doležal. Experimental methods of nuclear and subnuclear physics. http://ipnp.cz/~dolezal/teach/expmet/expmet.pdf. [2020-12-07].

[15] R.F.H. Hunter. *Development and evaluation of novel, lagre area, radiation hard silicon microstrip sensors for the ATLAS ITk experiment at the HL-LHC.* PhD thesis, Carleton University, 08 2017.

[16] Microsoft visual studio. https://visualstudio.microsoft.com/cs/. [cited 2020-17-09].

[17] ROOT. https://root.cern.ch/. [cited 2020-17-09].

[18] Translation stages. http://www.standa.lt/products/catalog/motorised_positioners?item=64&prod=motorized_translation_stage. [cited 2020-18-09].

[19] TTi documentation sheet. https://www.tme.eu/Document/660058b7f24f4d50e8bee95a285ac01e/CPX400SP.pdf. [cited 2020-17-09].

List of Figures

List of Tables

List of Abbreviations

3PG	Three Point gain
AD	Antiproton Decelerator
ALICE	A Lagre Ion Collider Experiment
ATLAS	A Toroidal LHC ApparatuS
AWAKE	Advanced Wakefield Experiment
CENF	CErn Neutrino platForm
CERN	Conseil Europèen pour la Recherche Nuclèaire
CHARM	Cern High energy AcceleRator Mixed field facility
CMS	Compact Muon Solenoid
CR1	Clean Room 1
CTF3	Clic Test Facility
DAQ	Data AcQuisition
GIF++	Gamma Irradiation Facility
HiRadMat	High-Radiation to Materials
HL-LHC	High Luminosity Large Hadron Collider
Html	HyperText Markup Language
Http	HyperText Transfer Protocol
ID	Inner Detector
IPNP	Institute of Particle and Nuclear Physic
IRRAD	proton IRRADioation facility
ISOLDE	Isotope Separator OnLine
ITk	Inner TracKer
ITSDAQ	Inner TracKer Data AcQuisition
LEAR	Low Energy Antiproton Ring
LEIR	Low Energy Ion Ring
LHC	Large Hadron Colider
LHCb	Large Hadron Collider Beauty
LiAr	Liquid Argon calorimeter
LINAC	LINear ACcelerator
MOS	Metal Oxide Semiconductor
MSVC	MicroSoft Visual C++
n-ToF	Neutrons Time Of Flight
NA	North Area
PS	Super Proton Synchrotron
RC	Response Curve
REX/HIE	Radioactive EXperiment/High Intensity and Energy ISOLDE
SC	Synchrocyclotron

SN	Signal to Noise ratio
SPS	Super Proton Synchrotron
TileCal	Tile Calorimeter
TRT	Transition Radiation Tracker
URL	A Uniform Resource Locator
USB	Universal Serial Bus
vt50	Value of Threshold at 50% maxima